Hydrodynamic dispersion and diffusivity contrast govern the stability of a reaction front in porous media

Gourab Chakraborty, Vinod Narayanan, and Uddipta Ghosh*
Department of Mechanical Engineering, Indian Institute of Technology Gandhinagar, Palaj, Gandhinagar 382055, Gujarat, India

(Received 29 January 2026; accepted 24 July 2026; published 17 August 2026)

Viscous fingering instabilities occurring at reactive mixing interfaces prevailing in porous media are often driven by concentration-dependent viscosity of the constituent fluids and play a vital role in several environmental and industrial processes. The stability of such reaction fronts is usually modeled at the Darcy scale, often under the pretense of a constant and identical molecular diffusivity of both the reactants and the product. However, at the Darcy scale, evolution of mixing interfaces is generally governed by hydrodynamic dispersion rather than molecular diffusion, while the diffusion coefficients of the various species involved are often distinct. Yet, their impact on the stability of a reaction front remains hitherto unexplored. As such, in this article we perform a linear stability analysis to unravel the role of dispersion on the stability of a bimolecular reaction front with regards to viscous fingering, where all species have distinct molecular diffusivities. The dispersion tensor is assumed to be linearly dependent on the local Darcy velocity, and the viscosity is assumed to vary exponentially with species concentrations. The stability of the front is analyzed using a transient approach where an initial value problem (IVP) is solved for the perturbations. A second approach using a quasi-steady-state approximation (QSSA) is also adopted as a reference case. We show that although the results from QSSA and IVP eventually converge at sufficiently large times, significant differences persist during the early stages, depending on the precise nature of viscosity variation. In particular, the results from the IVP approach show that both longitudinal and transverse dispersion tend to suppress the growth of perturbations. We further establish that the stability characteristics of the front become independent of the ratio between diffusion-to-advection timescales (the Péclet number) when hydrodynamic dispersion is taken into account. We demonstrate that diffusivity contrast between the product and the reactants may suppress or promote instability. Notably, it is shown that enhanced diffusivity of the product in scenarios where it is the most viscous element may stabilize an otherwise unstable front. The results shown here may be relevant to applications such as contaminant remediation, enhanced oil recovery, and carbon sequestration.

DOI: 10.1103/fd77-rd4d

I. INTRODUCTION

Reactive fronts that form at the interface between two miscible and reacting fluids are omnipresent in subsurface porous media and influence a wide range of operations such as groundwater and contaminant remediation [1–3], enhanced oil recovery [4–6], and carbon sequestration [7–10], alongside several other geochemical processes [11–16]. For instance, when injected plumes of chemically active agents come into contact with the resident contaminants in the subsurface,

*Contact author: uddipta.ghosh@iitgn.ac.in

reaction fronts naturally develop and move with the imposed flow. The extent of decontamination thus strongly depends on the rate of mixing and reaction in these fronts, which in turn depends on the underlying flow and the spatiotemporal evolution of the interface. As a result, stability of the reaction front becomes crucial in such processes, as they often control the shape and thereby the mixing rate at the interface.

It has long been recognized [17–22] that reactive mixing in porous media can alter local fluid properties such as viscosity, density, and surface tension, which may destabilize the very fronts where these reactions take place. For instance, chemical reactions may locally alter the viscosity of the fluid, which may trigger a viscous fingering (VF) instability [18,19,22], leading to fingerlike patterns at the mixing interface. Indeed, such patterns are known to appear frequently in secondary and tertiary oil recovery [4] when crude oil is displaced by water, the latter being less viscous than the former. Similar instabilities also occur when CO_2 is injected into the subsurface for the purpose of sequestration [7] and undergoes dissolution in brine water and subsequent chemical reactions with minerals. Motivated by the above implications of VF instabilities in reaction fronts, considerable effort has been put in to understand how they are triggered in the presence of chemical reactions, using experimental [18,19,23–25], theoretical [25–30], and numerical [31–40] tools. Nagatsu *et al.* [18] experimentally demonstrated that reactions can indeed modify the local viscosity, which can instigate VF instabilities and impact the physico-chemical characteristics of the fingers thus formed. On the numerical front, Gérard and De Wit [33] verified the VF patterns observed experimentally by Podgorski *et al.* [23], taking into account the distinct diffusivities of the various reacting species. From a theoretical standpoint, Hejazi *et al.* [26] performed a linear stability analysis of a miscible $A + B \rightarrow C$-type reaction front. They established that chemical reactions may render an originally stable mixing interface (a viscous fluid displacing a less viscous one) unstable by altering the local composition of the fluid, wherein the viscosity gradients become reversed. Later, Sharma *et al.* [30] extended the linear stability analysis to miscible reactive fronts in radial flows and reported that the onset of instability depends on both the reaction rate and the viscosity contrast.

Despite the attention received by VF instabilities, a few common missing traits may be found in almost all prior investigations, mainly because of the underlying assumptions. First and most importantly, most previous studies on reactive viscous fingering, especially those on bimolecular reactions, have considered reactive transport under constant molecular diffusivities, a paradigm that often becomes invalid in porous media. This is because transport in porous media is often described at the Darcy scale [12,41], which is indeed the smallest scale where upscaled equations of flow and transport retain their applicability. Modeling at the Darcy scale remains invaluable for the physical insights it provides without necessarily delving into the pore-scale features which may be computationally prohibitive in most porous media of practical interest. However, the pore-scale heterogeneities in the concentrations and velocity do leave their mark on the Darcy scale description of solute transport through hydrodynamic dispersion [41–43], which directly stems from the pore-scale coupling between advection and molecular diffusion. Hydrodynamic dispersion is generally expressed as a second rank tensor linearly dependent on the local Darcy velocity [41,44]. In most cases of practical interest, it acts as the dominant mixing mechanism over pure molecular diffusion [45]. As such, recent studies have revealed that hydrodynamic dispersion may strongly influence the mixing processes, qualitatively altering key metrics like reaction rate, front progression, and width [46–52]. It is thus not difficult to imagine that they might also have a significant role to play with regard to reactive VF instabilities [39,53–55], instigated by such processes.

Second, most theoretical attempts toward linear stability analysis of viscous fingering in reaction fronts assume the molecular diffusivities of all species to be identical (although purely numerical studies do not make such assumptions). This assumption is made because it simplifies the governing equations to a considerable extent [26,30] as far as linear stability is concerned, but is almost always violated in practice. In fact, diffusivity differences may be a key factor in controlling the local property variations close to the front [56], as it determines the relative mobility of the various species involved. This, in turn, may alter the stability characteristics of the underlying reactive fronts, although its precise impact remains an open question to a large extent.

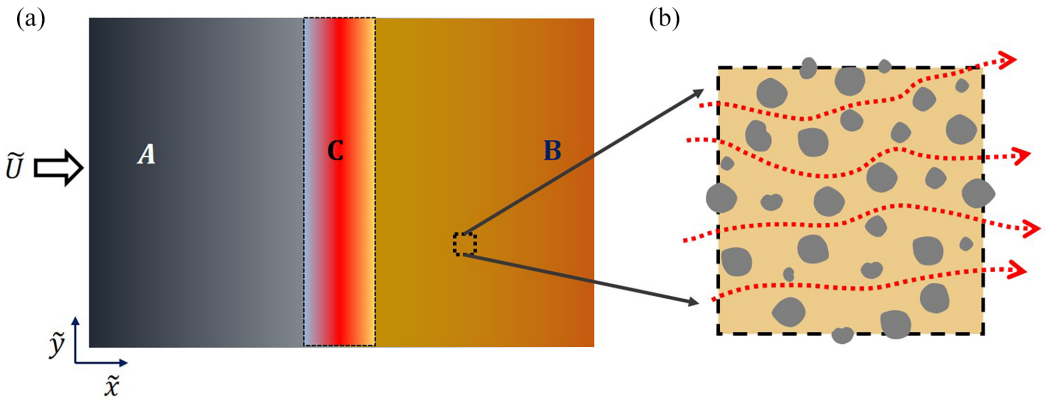

FIG. 1. (a) Schematic of the reactive front under consideration. Species A is injected at a constant speed $\tilde{U}$ from the left, confronts the resident species B, and forms a reactive mixing front producing C. (b) A magnified view of the underlying porous media through which the flow and transport takes place. As fluid flows through the tortuous pathways of the pore structure, fluid particles experience a spatially variable velocity field (shown by dotted red lines) leading to enhanced mixing of the solute at the macroscale, which is quantified by hydrodynamic dispersion.

In this article, we attempt to address the outstanding issues described above by carrying out a linear stability analysis of a miscible bimolecular ($A + B \rightarrow C$) reactive front in the presence of hydrodynamic dispersion. The molecular diffusivities of the reactants and the product are considered to be distinct, which, as we show later, increases the computational cost to a limited extent. We have chosen a bimolecular reaction for its relative simplicity and its relevance in representing various reactions (such as precipitation [57,58] and oxidation [59,60]) with a reasonable degree of accuracy. We consider the reactant A to be displacing reactant B in a porous media, propelled by an initially uniform flow field. Both the reactants and the product locally change the viscosity of the fluid, thereby fueling the instability. The framework used here is based on the advection-dispersion-reaction equations (ADREs) for the solute species, coupled with the Darcy flow equation. We show that the presence of hydrodynamic dispersion dampens the growth of perturbations when compared to pure molecular diffusion whereas, depending on the nature of the viscosity profile, diffusivity contrast may both amplify and dampen the growth of those perturbations.

The rest of this article is organized as follows. Section II provides a detailed description of the reactive system under consideration and the relevant governing equations. Section III outlines the linear stability framework and some key features of the numerical scheme used. In Sec. IV, results of the linear stability analysis are presented with an emphasis on the impact of dispersion and diffusivity contrast. Finally, the study is concluded with Sec. V.

II. PROBLEM FORMULATION AND GOVERNING EQUATIONS

A. Physical description of the system and the key assumptions

We consider a two-dimensional saturated porous medium, depicted schematically in Fig. 1. Initially, the entire medium is filled with a solution of species B, whose viscosity is $\tilde{\mu}_B$. A solution of species A (dissolved in the same fluid) with viscosity $\tilde{\mu}_A$ is continuously injected from the left at a constant speed $\tilde{U}\hat{\mathbf{e}}_x$ along the $\tilde{x}$ axis (see figure). For convenience, we shall assume the initial concentrations of both A and B to be identical to $\tilde{a}_0$, and the viscosity values of their solutions mentioned above pertain to this particular concentration. The two (miscible) solutions meet and form a moving front (moving to the right with velocity $\tilde{U}$), where a bimolecular $A + B \rightarrow C$ chemical reaction takes place between the two species. The product C alters the viscosity of the

fluid; when only species C is dissolved with concentration $\tilde{a}_0$, the fluid's viscosity becomes $\tilde{\mu}_C$, which is generally assumed to be distinct from those of the reactants. Therefore, the reactive mixing process at the front will alter the local concentrations of A, B, and C because of which the local viscosity ($\tilde{\mu}$) will vary depending on the concentrations of the three species. The reactants and the products may also alter other fluid properties such as density. Such property variations may be seamlessly integrated within the current framework, although they will not be considered in this article.

When $\tilde{\mu}_A > \tilde{\mu}_B$ and no reactions take place, the mixing front between A and B moves stably and widens because of hydrodynamic dispersion. However, the presence of a reaction product with a distinct viscosity may make the reaction front between A and B unstable, depending on the relative magnitudes of $\tilde{\mu}_A$, $\tilde{\mu}_C$, and $\tilde{\mu}_B$. On the other hand, if $\tilde{\mu}_A < \tilde{\mu}_B$, the front will be inherently susceptible to viscous fingering instabilities, and the presence of a product may further facilitate or suppress the ensuing instabilities.

In what follows, we shall adopt a Darcy-scale description of the flow and transport [41]. As such, it will be assumed that the permeability of the medium $\tilde{K}$ is uniform and identical for all species. The instantaneous reaction rate at the Darcy scale is given by $\tilde{R}\tilde{C}_A(\tilde{\mathbf{x}}, t)\tilde{C}_B(\tilde{\mathbf{x}}, t)$, where $\tilde{R}$ is the rate constant and $\tilde{C}_i(\tilde{\mathbf{x}}, t)$ ($i \equiv A,\ B$) is the local (Darcy scale) concentration of the ith species.

B. The hydrodynamic dispersion tensor

Hydrodynamic dispersion is the telltale sign of the pore-scale fluctuations in the velocity and species concentrations on the Darcy-scale description of solute transport [41,43,61]. Upon averaging the species conservation equation over a representative elementary volume, the combination of pore-scale fluctuations in velocity and concentration from their respective averages give rise to an undetermined additional flux [41,61]. This additional flux, which leads to a closure problem, also results in enhanced mixing of the dissolved species when viewed at an upscaled level (i.e., at the Darcy scale). It is quantified as a Fickian diffusive flux, linearly proportional to the local rate of discharge and the upscaled concentration's gradient [41,42,44,61]. It is distinct from Taylor dispersion [61,62] in that the former is caused by an incomplete mixing within the pores because of the limited residence time of the dissolved species therein. At the same time, molecular diffusion also acts in tandem to aid mixing in porous media. The total hydrodynamic dispersion is thus a combination of contributions from molecular diffusion and mechanical dispersion and, for an isotropic and homogeneous porous medium at the Darcy scale, it is expressed as a second rank symmetric tensor as follows [41,61]:

$$\tilde{\mathbf{D}}_i = \tilde{\mathbf{D}}_{\mathrm{M},i} + (\ell_L - \ell_T)\frac{\tilde{\mathbf{u}} \otimes \tilde{\mathbf{u}}}{|\tilde{\mathbf{u}}|} + \ell_T |\tilde{\mathbf{u}}| \mathbf{I}. \tag{1}$$

In the above, $\tilde{\mathbf{D}}_{\mathrm{M},i} = \tilde{D}_{\mathrm{M},i}\tilde{\mathbf{T}}$ is the effective molecular diffusion tensor of the ith species, where $\tilde{D}_{\mathrm{M},i}$ is the molecular diffusivity of that species and $\tilde{\mathbf{T}}$ is the tortuosity tensor, and $\mathbf{I}$ is the identity matrix. In the rest of this article, the molecular diffusivities of various species have been considered to be distinct, while the tortuosity tensor has been taken to be uniform and isotropic, i.e., $\tilde{\mathbf{T}} = \lambda\mathbf{I}$, λ being a constant. Therefore, $\tilde{\mathbf{D}}_{\mathrm{M},i} = \tilde{D}_{\mathrm{M,eff},i}\mathbf{I}$, where $\tilde{D}_{\mathrm{M,eff},i} = \tilde{D}_{\mathrm{M},i}\tilde{\lambda}$ is the effective molecular diffusivity of species i. Furthermore, in Eq. (1), ℓ_L and ℓ_T, respectively, represent the longitudinal and transverse dispersion lengths (the factor of porosity may be absorbed within them), and their values depend on both the geometry at the pore scale and the pore sizes. The longitudinal dispersion length determines the approximate rate of spreading along the direction of flow, while the transverse one determines the spreading rate in a perpendicular direction. When $\ell_L = \ell_T$, one ends up with isotropic dispersion which entails an identical rate of spreading in all directions. However, usually, $\ell_L > \ell_T$ in most porous media. Finally, $\tilde{\mathbf{u}}$ is the local discharge rate of the fluid inside the porous media, and $|\tilde{\mathbf{u}}|$ represents its magnitude.

C. The governing equations for flow and transport at Darcy scale

The flow within the porous medium is governed by the continuity equation along with Darcy's law [41,43], which couples the discharge rate to the local pressure gradient. On the other hand, transport of the various reactive species are governed by the ADREs [41,43]. These may be expressed mathematically as follows:

$$\tilde{\boldsymbol{\nabla}} \cdot \tilde{\mathbf{u}} = 0, \quad \text{where} \quad \tilde{\mathbf{u}} = -\frac{\tilde{K}}{\tilde{\mu}(\tilde{C}_A, \tilde{C}_B, \tilde{C}_C)} \tilde{\boldsymbol{\nabla}} \tilde{p}, \tag{2a}$$

$$\frac{\partial \tilde{C}_i}{\partial \tilde{t}} + \tilde{\mathbf{u}} \cdot \tilde{\boldsymbol{\nabla}} \tilde{C}_i = \tilde{\boldsymbol{\nabla}} \cdot (\tilde{\mathbf{D}}_i \cdot \tilde{\boldsymbol{\nabla}} \tilde{C}_i) - \tilde{R} \tilde{C}_A \tilde{C}_B, \quad i \equiv A, B, \tag{2b}$$

$$\frac{\partial \tilde{C}_C}{\partial \tilde{t}} + \tilde{\mathbf{u}} \cdot \tilde{\boldsymbol{\nabla}} \tilde{C}_C = \tilde{\boldsymbol{\nabla}} \cdot (\tilde{\mathbf{D}}_C \cdot \tilde{\boldsymbol{\nabla}} \tilde{C}_C) + \tilde{R} \tilde{C}_A \tilde{C}_B, \tag{2c}$$

where $\tilde{\mathbf{u}} = \tilde{u}\hat{\mathbf{e}}_x + \tilde{v}\hat{\mathbf{e}}_y$ is the Darcy scale velocity (i.e., the discharge rate), $\tilde{K}$ is the permeability of the medium, $\tilde{p}$ is the upscaled (Darcy scale) pressure, and $\tilde{R}$ is the reaction rate constant. Further, $\tilde{\mathbf{D}}_i$ is the hydrodynamic dispersion tensor of the ith species ($i \equiv A$, B, and C), given by Eq. (1). Evidently, all of Eqs. (2) are strongly coupled, simply because the viscosity $\tilde{\mu}$ depends on the concentrations of the reactants ($\tilde{C}_A$ and $\tilde{C}_B$) as well as the product ($\tilde{C}_C$), while the dispersion tensor depends on the local velocity. Several previous studies [31,33,39,63] have taken the dependence of viscosity on species concentrations to be exponential, and here also we shall take a similar form, which reads

$$\tilde{\mu}(\tilde{C}_A, \tilde{C}_B, \tilde{C}_C) = \tilde{\mu}_s e^{(R_A \tilde{C}_A + R_B \tilde{C}_B + R_C \tilde{C}_C)/\tilde{a}_0}, \tag{3}$$

where R_A, R_B, and R_C are known as the log-mobility ratios and are defined as

$$R_A = \ln\left(\frac{\tilde{\mu}_A}{\tilde{\mu}_s}\right), \quad R_B = \ln\left(\frac{\tilde{\mu}_B}{\tilde{\mu}_s}\right), \quad \text{and} \quad R_C = \ln\left(\frac{\tilde{\mu}_C}{\tilde{\mu}_s}\right). \tag{4}$$

In Eqs. (4), $\tilde{\mu}_A$, $\tilde{\mu}_B$, and $\tilde{\mu}_C$, respectively, represent the viscosity of the solution when only one species, i.e., either A or, B or, C is present at a concentration $\tilde{a}_0$, and $\tilde{\mu}_s$ is the viscosity of the pure fluid permeating the porous medium in the absence of any solute. Thus, $R_B - R_A > 0$ will indicate that a less viscous solution is displacing a more viscous one (vice versa for $R_B - R_A < 0$), while $R_C - R_A > 0$ will indicate that the product makes the solution more viscous as compared to the injected species. When $R_C - R_A > R_B - R_A > 0$, the reaction front becomes the most viscous part of the solution. One may also realize that any other property variations with respect to species concentrations, such as that of density or permeability may also be easily incorporated within the above description. However, such variations will only add to an already large set of tunable parameters as we demonstrate shortly, and hence are not accounted for in this article.

It may be convenient to make a change of reference frame that moves with the injection velocity $\tilde{U}\hat{\mathbf{e}}_x$. In this moving frame, the spatial coordinates transform as

$$\tilde{\mathbf{x}}' = \tilde{\mathbf{x}} - \tilde{U}\tilde{t}\hat{\mathbf{e}}_x. \tag{5}$$

In addition, the base velocity in this frame vanishes, i.e., $\tilde{\mathbf{u}}' = \mathbf{0}$. We emphasize that spatial coordinates and the velocity in this moving frame are denoted with a prime, while species concentrations ($\tilde{C}_i$) [and also time ($\tilde{t}$)] do not need to be transformed as they are scalars and hence have the same definitions in either coordinates.

In the moving frame, the set of Eqs. (2) are subject to the following initial conditions (at $\tilde{t} = 0$):

$$\tilde{C}_A = \begin{Bmatrix} \tilde{a}_0 & \tilde{x}' < 0 \\ 0 & \tilde{x}' > 0 \end{Bmatrix}, \quad \tilde{C}_B = \begin{Bmatrix} 0 & \tilde{x}' < 0 \\ \tilde{a}_0 & \tilde{x}' > 0 \end{Bmatrix}, \quad \tilde{C}_C = 0. \tag{6}$$

The spatial extent of the domain along both $\tilde{x}$ and $\tilde{y}$ are considered to be infinite, which simply means that all physical quantities must remain bounded as one approaches infinity in all directions.

TABLE I. Characteristics scales used to nondimensionalize the relevant quantities.

Variable	Characteristic scale	Remarks
Velocity ($\tilde{\mathbf{u}}$)	$\tilde{U}$	Injection speed
Time ($\tilde{t}$)	$1/(\tilde{R}\tilde{a}_0)$	Reaction timescale
Length ($\tilde{\mathbf{x}}$)	$\tilde{U}/(\tilde{R}\tilde{a}_0)$	Injection speed times the timescale
Pressure ($\tilde{p}$)	$\tilde{\mu}_s\tilde{U}^2/\tilde{R}\tilde{a}_0\tilde{K}$	
Viscosity ($\tilde{\mu}$)	$\tilde{\mu}_s$	$\tilde{\mu}(\tilde{C}_A = 0, \tilde{C}_B = 0, \tilde{C}_C = 0)$
Concentrations ($\tilde{C}_i$)	$\tilde{a}_0$	Initial concentration of the reactants

D. Dimensionless governing equations

Hereon, we shall only deal with dimensionless forms of all variables and equations. To this end, the nondimensional version of any variable, say $\tilde{\Psi}$, is expressed as $\Psi = \tilde{\Psi}/\Psi_c$ (the tilde is dropped), where Ψ_c is the characteristic scale of the said variable. The characteristic scales for all variables are shown in Table I. While the choice of scales for velocity, viscosity, and concentration are straightforward, a few words are necessary on the choice of the time and length scales. First, we recognize that the only natural timescale in the problem is the reaction time denoted as $t_c = (\tilde{R}\tilde{a}_0)^{-1}$ which is also chosen as the characteristic timescale. This helps us define a length scale as $l_c = \tilde{U}/\tilde{R}\tilde{a}_0$, using which a pressure scale may also be defined, as noted in Table I.

Upon enforcing the nondimensionalization scheme described above, Eqs. (2) take the following form in the coordinate moving with the front [see Eq. (5)]:

$$\nabla \cdot \mathbf{u}' = 0, \quad \text{where} \quad \mathbf{u}' + \hat{\mathbf{e}}_x = -\frac{1}{\mu}\nabla p, \tag{7a}$$

$$\frac{\partial C_i}{\partial t} + \mathbf{u}' \cdot \nabla C_i = \nabla \cdot (\mathbf{D}_i \cdot \nabla C_i) - C_A C_B, \quad i \equiv A, B \tag{7b}$$

$$\frac{\partial C_C}{\partial t} + \mathbf{u}' \cdot \nabla C_C = \nabla \cdot (\mathbf{D}_C \cdot \nabla C_C) + C_A C_B, \tag{7c}$$

where $\nabla = \hat{\mathbf{e}}_x \frac{\partial}{\partial x'} + \hat{\mathbf{e}}_y \frac{\partial}{\partial y'}$ now denotes the gradient operator in moving (x', y') coordinates. The hydrodynamic dispersion tensor for the ith species after nondimensionalization takes the form

$$\mathbf{D}_i = \frac{\Lambda_i}{\mathrm{Pe}}\mathbf{I} + (\eta_L - \eta_T)\frac{\mathbf{u} \otimes \mathbf{u}}{|\mathbf{u}|} + \eta_T |\mathbf{u}|\mathbf{I}, \tag{8}$$

where $\eta_L = (\ell_L \tilde{R}\tilde{a}_0)/\tilde{U}$ and $\eta_T = (\ell_T \tilde{R}\tilde{a}_0)/\tilde{U}$ are, respectively, the dimensionless longitudinal and transverse dispersion lengths, and $\Lambda_i = \tilde{D}_{\mathrm{Meff,i}}/\tilde{D}_{\mathrm{Meff,A}}$ denotes the diffusivity ratios; evidently, $\Lambda_A = 1$. It is important to note that in Eq. (8), the dispersion tensor is defined in terms of the total velocity $\mathbf{u} = \mathbf{u}' + \hat{\mathbf{e}}_x$ (and not the velocity in the moving frame). One other important nondimensional number appears in this equation, which is the Péclet number (Pe) representing the ratio of the diffusion timescale to the advection timescale, and is expressed as $\mathrm{Pe} = \tilde{U}^2/(\tilde{R}\tilde{a}_0\tilde{D}_{\mathrm{M,eff,A}})$. Usually, in reactive transport problems, one may also define a Damköhler number (Da) [26,35,38], which entails the ratio of the diffusion timescale to the reaction timescale. However, here the advection time (i.e., $l_c/u_c = l_c/\tilde{U}$) is identical to the reaction timescale, and thus Da = Pe in all cases. One may thus think of the coefficient to the last terms in Eqs. (7b) and (7c) as being Da/Pe, which becomes unity upon enforcing our nondimensionalization scheme. It is also interesting to note that a relatively faster reaction will result in a relatively larger Pe (and thus also Da), and a relatively smaller η_L and η_T, with all other variables kept unchanged. Therefore, dispersion seems to have weaker impact on relatively faster reactions.

The dimensionless viscosity now has the following expression:

$$\mu(C_A, C_B, C_C) = e^{R_A C_A + R_B C_B + R_C C_C}. \tag{9}$$

Finally, the initial conditions remain similar to Eqs. (6) with $\tilde{a}_0$ replaced with 1, and other variables replaced with their dimensionless counterparts.

Since most prior studies consider the reactants and the product to have identical molecular diffusivities, it may be worth noting the key simplifications it entails as compared to the present framework. First and foremost, when $\Lambda_A = \Lambda_B = \Lambda_C = 1$, it directly follows from Eqs. (7) that $\Xi = C_A(\mathbf{x}, t) + C_B(\mathbf{x}, t) + 2C_C(\mathbf{x}, t) = 1$ remains a conserved quantity everywhere [26]. Therefore, one only needs to solve for any two of the species concentrations, and the concentration of the third species is then evaluated using the relation $\Xi = 1$. It is obvious that this simplification is not applicable when the molecular diffusivities become distinct, and one needs to separately solve for the concentrations of all three species, which increases the computational load. Second, it may be shown [26] that for $\tilde{D}_{M,A} = \tilde{D}_{M,B} = \tilde{D}_{M,C}$, Eq. (9) may be simplified to the following form without loss of generality: $\mu = e^{R_B^* C_B + R_C^* C_C}$, i.e., the dependence of viscosity on C_A may be dropped explicitly. This is another subtle difference between the present scenario and that of the identical diffusivity.

III. LINEAR STABILITY ANALYSIS OF THE REACTIVE FRONT

A. The base state

In linear stability analysis, instantaneous variations in the species concentration and the velocity are expressed as the sum of the base state (unperturbed) solution and the perturbations as follows:

$$C_i(x', y', t) = C_{i,0}(x', t) + \hat{C}_i(x', y', t), \quad i \equiv A, B, C, \tag{10a}$$

$$p(x', y', t) = p_0(x', t) + \hat{p}(x', y', t), \tag{10b}$$

$$\mu(x', y', t) = \mu_0(x', t) + \hat{\mu}(x', y', t), \tag{10c}$$

$$\mathbf{u}'(x', y', t) = \hat{\boldsymbol{u}}(x', y', t). \tag{10d}$$

In the above, the quantities with subscript 0 denote the base state, and the hatted entities $\hat{(\cdot)}$ denote the perturbation components of those respective base values. It is to be noted that in the moving coordinate, the base velocity is identically zero and therefore $\mathbf{u}' = \hat{\boldsymbol{u}} = \hat{u}(x', y', t)\hat{\mathbf{e}}_x + \hat{v}(x', y', t)\hat{\mathbf{e}}_y$.

When the flow is unperturbed and no transverse disturbances are present, the velocity field remains uniform, and the species concentrations depend solely on x' and t. Under these conditions, the governing equations for the base concentrations reduce to ordinary reaction-diffusion type equations, given by

$$\frac{\partial C_{A,0}}{\partial t} = \left(\frac{1}{\mathrm{Pe}} + \eta_L\right)\frac{\partial^2 C_{A,0}}{\partial x'^2} - C_{A,0}C_{B,0}, \tag{11a}$$

$$\frac{\partial C_{B,0}}{\partial t} = \left(\frac{\Lambda_B}{\mathrm{Pe}} + \eta_L\right)\frac{\partial^2 C_{B,0}}{\partial x'^2} - C_{A,0}C_{B,0}, \tag{11b}$$

$$\frac{\partial C_{C,0}}{\partial t} = \left(\frac{\Lambda_C}{\mathrm{Pe}} + \eta_L\right)\frac{\partial^2 C_{C,0}}{\partial x'^2} + C_{A,0}C_{B,0}. \tag{11c}$$

A concise derivation of the above equations have been included in Appendix A. The initial condition for the above set of equations is

$$C_{A,0} = \begin{Bmatrix} 1 & x' < 0 \\ 0 & x' > 0 \end{Bmatrix}, \quad C_{B,0} = \begin{Bmatrix} 0 & x' < 0 \\ 1 & x' > 0 \end{Bmatrix}, \quad C_{C,0} = 0. \tag{12}$$

The base state viscosity profile on the other hand is given by $\mu_0 = e^{R_A C_{A,0} + R_B C_{B,0} + R_C C_{C,0}}$.

It is important to note here that the base state itself is unsteady—the concentrations evolve spatially and temporally as the reaction progresses. Therefore, it is expected that the stability characteristics of the front may also evolve with time, depending on how the three species impact the local viscosity of the solvent.

B. Linearized equations for the perturbations

In an effort to derive the governing equations for the perturbations to the concentrations and velocity, we substitute the variable forms given in Eqs. (10) into Eqs. (7b) and (7c), use the equations satisfied by the base state solutions [i.e., Eqs. (11a)–(11c)], and ignore all nonlinear terms involving the perturbations (as per the norms of linear stability analysis). As such, we arrive at the following linearized equations governing the perturbations in the reactant ($\hat{C}_A$ and $\hat{C}_B$) and the product concentrations ($\hat{C}_C$):

$$\frac{\partial \hat{C}_i}{\partial t} + \hat{u}\frac{\partial C_{i,0}}{\partial x'} = \left(\left(\frac{\Lambda_i}{\mathrm{Pe}} + \eta_L\right)\frac{\partial^2}{\partial x'^2} + \left(\frac{\Lambda_i}{\mathrm{Pe}} + \eta_T\right)\frac{\partial^2}{\partial y'^2}\right)\hat{C}_i + \eta_L\left(\hat{u}\frac{\partial^2 C_{i,0}}{\partial x'^2} + \frac{\partial \hat{u}}{\partial x'}\frac{\partial C_{i,0}}{\partial x'}\right) - (\eta_L - \eta_T)\frac{\partial \hat{u}}{\partial x'}\frac{\partial C_{i,0}}{\partial x'} - (\hat{C}_A C_{B,0} + C_{A,0}\hat{C}_B) \quad i \equiv A, B, \tag{13a}$$

$$\frac{\partial \hat{C}_C}{\partial t} + \hat{u}\frac{\partial C_{C,0}}{\partial x'} = \left(\left(\frac{\Lambda_C}{\mathrm{Pe}} + \eta_L\right)\frac{\partial^2}{\partial x'^2} + \left(\frac{\Lambda_C}{\mathrm{Pe}} + \eta_T\right)\frac{\partial^2}{\partial y'^2}\right)\hat{C}_C + \eta_L\left(\hat{u}\frac{\partial^2 C_{C,0}}{\partial x'^2} + \frac{\partial \hat{u}}{\partial x'}\frac{\partial C_{C,0}}{\partial x'}\right) - (\eta_L - \eta_T)\frac{\partial \hat{u}}{\partial x'}\frac{\partial C_{C,0}}{\partial x'} + (\hat{C}_A C_{B,0} + C_{A,0}\hat{C}_B). \tag{13b}$$

Similarly, the linearized expression for the perturbation in viscosity ($\hat{\mu}$) is given by $\hat{\mu} = (R_A\hat{C}_A + R_B\hat{C}_B + R_C\hat{C}_C)\mu_0$ (again, neglecting nonlinear contributions).

Equations governing the perturbations to the velocity may be derived using Eq. (7a). We take curl of the Darcy's equation [second of Eq. (7a)], use the continuity equation ($\boldsymbol{\nabla}\cdot\mathbf{u}' = 0$) together with the perturbed viscosity as mentioned above, and subsequently arrive at the following linearized equation governing the perturbation $\hat{u}(\mathbf{x}', t)$:

$$\left(\frac{\partial^2}{\partial x'^2} + \frac{\partial^2}{\partial y'^2}\right)\hat{u} + \frac{1}{\mu_0}\frac{\partial \mu_0}{\partial x'}\frac{\partial \hat{u}}{\partial x'} = -R_A\frac{\partial^2 \hat{C}_A}{\partial y'^2} - R_B\frac{\partial^2 \hat{C}_B}{\partial y'^2} - R_C\frac{\partial^2 \hat{C}_C}{\partial y'^2}. \tag{14}$$

It is interesting to note that although the base state concentrations are only governed by longitudinal dispersion (η_L), the perturbations and hence the stability of the front depends on both transverse (η_T) and longitudinal dispersion lengths. Because the base-state variables themselves evolve in time, solving the above linearized equations and evaluating the growth rates becomes nontrivial. In particular, at early times, the base state evolves rapidly due to the relatively large concentration gradients near the front. As a result, it is essential to account for its temporal evolution to accurately capture the growth rates of the disturbances and the associated instability regions [64–68]. However, as time progresses, the evolution of the base state becomes increasingly slower as the gradients weaken. Therefore, at later times, the above stability problem may be simplified by adopting a quasi-steady-state approach which treats the base state being effectively frozen—see the subsections ahead.

C. Transient stability framework—the initial value problem

Because of the unsteady nature of the base state, Tan and Homsy [63] noted that an appropriate way to compute the growth rate of the perturbations is to use a transient analysis, wherein an initial value problem (IVP) is solved for a given mode. Building upon their work, we resolve the perturbations using Fourier modes along the y direction as follows [69,70]:

$$[\hat{u}, \hat{C}_A, \hat{C}_B, \hat{C}_C] = [\phi(x', t), \psi_A(x', t), \psi_B(x', t), \psi_C(x', t)]e^{i\alpha y}, \tag{15}$$

where α is the wave number [69]. We emphasize that the above decomposition becomes possible because all coefficients in Eqs. (13) and (14) are independent of y. Furthermore, $\phi(x', t)$ and $\psi_i(x', t)$ ($i \equiv A, B, C$) represent the amplitude of the perturbations. Upon inserting the above Fourier mode

expansion into the linearized Eqs. (13a), (13b), and (14), and after a bit of algebra, we arrive at the following set of equations for the various amplitude functions for a specific mode:

$$\left\{\left(\frac{1}{\mathrm{Pe}}+\eta_L\right)\frac{\partial^2}{\partial x'^2}-\left(\frac{1}{\mathrm{Pe}}+\eta_T\right)\alpha^2-C_{B,0}\right\}\psi_A-C_{A,0}\psi_B + \left[\eta_L\left(\frac{\partial^2 C_{A,0}}{\partial x'^2}+\frac{\partial C_{A,0}}{\partial x'}\frac{\partial}{\partial x'}\right)-(\eta_L-\eta_T)\frac{\partial C_{A,0}}{\partial x'}\frac{\partial}{\partial x'}-\frac{\partial C_{A,0}}{\partial x'}\right]\phi=\frac{\partial \psi_A}{\partial t}, \tag{16a}$$

$$\left\{\left(\frac{\Lambda_B}{\mathrm{Pe}}+\eta_L\right)\frac{\partial^2}{\partial x'^2}-\left(\frac{\Lambda_B}{\mathrm{Pe}}+\eta_T\right)\alpha^2-C_{A,0}\right\}\psi_B-C_{B,0}\psi_A + \left[\eta_L\left(\frac{\partial^2 C_{B,0}}{\partial x'^2}+\frac{\partial C_{B,0}}{\partial x'}\frac{\partial}{\partial x'}\right)-(\eta_L-\eta_T)\frac{\partial C_{B,0}}{\partial x'}\frac{\partial}{\partial x'}-\frac{\partial C_{B,0}}{\partial x'}\right]\phi=\frac{\partial \psi_B}{\partial t}, \tag{16b}$$

$$\left\{\left(\frac{\Lambda_C}{\mathrm{Pe}}+\eta_L\right)\frac{\partial^2}{\partial x'^2}-\left(\frac{\Lambda_C}{\mathrm{Pe}}+\eta_T\right)\alpha^2\right\}\psi_C+C_{B,0}\psi_A+C_{A,0}\psi_B + \left[\eta_L\left(\frac{\partial^2 C_{C,0}}{\partial x'^2}+\frac{\partial C_{C,0}}{\partial x'}\frac{\partial}{\partial x'}\right)-(\eta_L-\eta_T)\frac{\partial C_{C,0}}{\partial x'}\frac{\partial}{\partial x'}-\frac{\partial C_{C,0}}{\partial x'}\right]\phi=\frac{\partial \psi_C}{\partial t}, \tag{16c}$$

$$\alpha^2(R_A\psi_A+R_B\psi_B+R_C\psi_C)=\left[\frac{\partial^2}{\partial x'^2}-\alpha^2+\left(R_A\frac{\partial C_{A,0}}{\partial x'}+R_B\frac{\partial C_{B,0}}{\partial x'}+R_C\frac{\partial C_{C,0}}{\partial x'}\right)\frac{\partial}{\partial x'}\right]\phi. \tag{16d}$$

In the above, the perturbations are subject to homogeneous Dirichlet conditions as $|x'|\to\infty$.

To capture the growth rates accurately, the above system of linear equations for the perturbation amplitudes (ϕ and ψ_i's) is solved directly as an IVP. Following Tan and Homsy [63], the initial condition for the disturbances is constructed using the eigenfunctions obtained from quasi-steady-state approximation (QSSA) analysis (see the subsection ahead) at $t=0$. It is important to note that here the resulting growth rates are functions of both space and time. In an effort to boil the growth rate down to a single quantity, we appeal to the square (energylike) norm of the perturbations ([63,66,67]), expressed as

$$\mathcal{Q}(t)=\iint(|\hat{u}|^2+|\hat{v}|^2+|\hat{C}_A|^2+|\hat{C}_B|^2+|\hat{C}_C|^2)dx'dy. \tag{17}$$

Upon substituting the expressions for the perturbations as mentioned in Eq. (15) into Eq. (17), and noting that the integration along the transverse direction yields a constant numerical factor which can be omitted without loss of generality, we arrive at the following:

$$\mathcal{Q}(t)=\int_{-\infty}^{\infty}\left(|\phi|^2+\left|\frac{i}{\alpha}\frac{\partial\phi}{\partial x'}\right|^2+|\psi_A|^2+|\psi_B|^2+|\psi_C|^2\right)dx'. \tag{18}$$

From the above, we can compute the instantaneous growth rate as follows [67]:

$$\omega(t)=\frac{1}{2}\frac{d}{dt}\ln(\mathcal{Q}(t)). \tag{19}$$

Although alternative measures for the growth rate are also available, it has been shown [63] that all of them largely result in values of ω very similar to that described in Eq. (19).

D. Linear stability analysis with the quasi-steady-state approach

It is evident that at large times, the rate of change of the base state slows down considerably. Therefore, at large times, the stability analysis can be performed under the QSSA [26], which provides a simpler and computationally efficient framework without compromising accuracy [63]. As per the QSSA [26], the base state evolves in time at a far slower rate than the perturbations, such that the former may be assumed to be frozen at a specific time, say t_0. This allows us to treat the base state as effectively being invariant in time while probing the growth of the underlying instabilities. As a consequence, the time appearing in the base state solutions through Eqs. (11) becomes a parameter (i.e., t_0) while analyzing the temporal evolution of the disturbances. With the above simplification, we may represent all perturbations using normal modes as follows [26,69,70]:

$$[\hat{u}, \hat{C}_A, \hat{C}_B, \hat{C}_C] = [\phi(x), \psi_A(x), \psi_B(x), \psi_C(x)]e^{i\alpha y+\omega(t_0)t}, \tag{20}$$

where $\omega(t_0) = \omega_r(t_0) + \omega_i(t_0)$ is the (complex) frequency with $\omega_r(t_0)$ being the growth rate, and $\omega_i(t_0)$ being the propagation speed of the disturbances [69]. Upon inserting Eq. (20) into the linearized Eqs. (13a), (13b), and (14), equations governing the amplitudes [i.e., $\phi(x)$ and $\psi(x)$'s) may be derived. The equations look very similar to those in Eqs. (16), except that the time derivatives of $\psi_i(x', t)$ ($i \equiv A, B, C$) are aptly replaced by $\omega\psi_i(x')$, and that all terms associated with the base state are evaluated at a fixed parametric time t_0. We do not furnish these equations here for brevity. The QSSA directly results in an eigenvalue problem with the complex frequency (ω) being the eigenvalue.

E. Numerical solutions to the linear stability equations

We have solved the coupled system of partial differential equations (16a)–(16d) numerically, using an implicit finite difference in time and Chebyshev spectral collocation method in space [71,72] to determine the transient evolution of the disturbances. The growth rate of the perturbations is subsequently evaluated based on Eq. (19). However, the standard Chebyshev–Lobatto grid is not suitable for the present scenario, simply because it naturally tends to cluster grid points near the boundaries which here lie at $\pm\infty$. In fact, the main action in the present scenario takes place near $x' = 0$ (i.e., near the front) and, hence, we should try to pack as many grid points as possible in the central region of the solution domain. To this end, we introduce a coordinate transformation that redistributes the grid points toward the central region and helps us capture the concentration and viscosity variations within the reaction front with a sharp resolution. At the same time, the computational domain must also be sufficiently wide to capture the essential variations, while ensuring that all perturbations appropriately decay at the far-field boundaries. As such, we take a truncated solution domain of half-length L ($\gg$1) and subsequently carry out the following transformation to redefine the independent spatial coordinate:

$$x_C^* = \frac{Lx_C}{1 + \beta\left(1 - x_C^2\right)}, \tag{21}$$

where $x_C \in [-1, 1]$ is the standard Chebyshev–Lobatto grid. Furthermore, β is a tuning parameter that controls the degree of grid stretching. This transformation concentrates grid points near $x' = 0$ (or, equivalently, $x_C^* = 0$), with the intensity of concentration becoming more pronounced as β increases.

The same Chebyshev spectral method described above is also used for solving the equations in the QSSA, which, upon discretization, may be reduced to a generalized eigenvalue problem of the form $\mathcal{A}\mathcal{X} = \omega\mathcal{B}\mathcal{X}$, where $\mathcal{X} = [\psi_A\ \psi_B\ \psi_C\ \phi]^T$, with ω as the eigenvalue and the amplitudes (i.e., $\psi_i,\ \phi$) are the corresponding eigenvectors. Given that both $\mathcal{A}$ and $\mathcal{B}$ have real entries, all complex eigenvalues (and eigenvectors) must appear as part of conjugate pairs. As per the QSSA, the reaction front is stable if $\omega_r < 0$ for all choices of the wave number (α), and unstable otherwise. It turns out that in the present scenario, $\omega_i = 0$ identically across all parameter ranges studied, suggesting that the resulting perturbations essentially behave as standing waves without propagating upstream or,

downstream. At this stage, the solutions to the IVP are difficult to validate directly. However, the growth rate predicted by the IVP approach may be validated against those from the QSSA at large times. The accuracy of the results from the QSSA in turn may be verified by comparing them with those from the existing literature, as shown in the subsection ahead.

F. Code validation

In an effort to validate our numerical solutions, we may compare the special case of our results pertaining to the absence of hydrodynamic dispersion ($\eta_L = \eta_T = 0$), with the findings of Hejazi *et al.* [26], who also performed a modal quasisteady stability analysis of a miscible $A + B \to C$ reactive front, subject to concentration-dependent viscosity variations. In their work, the characteristic length scale was chosen to be $l_{c,*} = \tilde{D}_{\mathrm{M,eff}}/\tilde{U}$ (the molecular diffusivity was assumed to be the same for all species in their work), from which $t_{c,*} = \tilde{D}_{\mathrm{M,eff}}/\tilde{U}^2$, leading to $\mathrm{Pe}_* = 1$. However, now the Damköhler number explicitly appears in the governing equations, defined as $\mathrm{Da}_* = \tilde{R}\tilde{a}_0\tilde{D}_{\mathrm{M,eff}}/\tilde{U}^2 = 1/\mathrm{Pe}$ (using the definition of the present work). As such, the linearized governing equations for the perturbations take the following form:

$$\boldsymbol{\nabla} \times (\mu_0 \hat{\boldsymbol{u}} + \hat{\mu}\hat{\mathbf{e}}_x) = 0 \quad \text{and} \quad \boldsymbol{\nabla} \cdot \hat{\boldsymbol{u}} = 0, \tag{22a}$$

$$\frac{\partial \hat{C}_i}{\partial t} + \hat{\boldsymbol{u}} \cdot \boldsymbol{\nabla} C_{i,0} = \boldsymbol{\nabla} \cdot (\hat{\mathbf{D}} \cdot \boldsymbol{\nabla} C_{i,0} + \mathbf{D}_{0,i} \cdot \boldsymbol{\nabla} \hat{C}_i) - \mathrm{Da}_*(\hat{C}_A C_{B,0} + C_{A,0}\hat{C}_B), \tag{22b}$$

$$\frac{\partial \hat{C}_C}{\partial t} + \hat{\boldsymbol{u}} \cdot \boldsymbol{\nabla} C_{C,0} = \boldsymbol{\nabla} \cdot (\hat{\mathbf{D}} \cdot \boldsymbol{\nabla} C_{C,0} + \mathbf{D}_{0,C} \cdot \boldsymbol{\nabla} \hat{C}_C) + \mathrm{Da}_*(\hat{C}_A C_{B,0} + C_{A,0}\hat{C}_B). \tag{22c}$$

In the above, $\mathbf{D}_{0,i} = (\Lambda_i + \eta_L)\hat{\mathbf{e}}_x\hat{\mathbf{e}}_x + (\Lambda_i + \eta_T)\hat{\mathbf{e}}_y\hat{\mathbf{e}}_y$ and $\hat{\mathbf{D}} = \hat{u}(\eta_L\hat{\mathbf{e}}_x\hat{\mathbf{e}}_x + \eta_T\hat{\mathbf{e}}_y\hat{\mathbf{e}}_y) + (\eta_L - \eta_T)\hat{v}(\hat{\mathbf{e}}_x\hat{\mathbf{e}}_y + \hat{\mathbf{e}}_y\hat{\mathbf{e}}_x)$ are, respectively, the base state component of the dispersion tensor for the ith species and the perturbation component of the dispersion tensor. We emphasize that the linearized equations derived in the present work [Eqs. (13) and (14)] become identical to the above upon writing the coefficient of the reaction terms as Da_*, and then enforcing $\mathrm{Pe} = 1$. At the same time, we shall enforce $R_A = 0$ to reproduce the viscosity profile taken in the work of Hejazi *et al.* Because of the differences in the choices of the time and length scales, in this subsection we shall denote the (QSSA) growth rate as ω_*, and the wavelength as α_* for the purposes of comparison. For purposes of validation, we have solved Eqs. (22) by setting $\eta_L = \eta_T = 0$, and then using the same Chebyshev spectral collocation method outlined in Sec. III E.

Figure 2 shows the comparison of the dispersion curves, i.e., the variations in ω_* as a function of α_* for various choices of log-mobility ratios (R_B and R_C), Damköhler numbers (Da_*), and time instances (t_0) between our results based on the QSSA (lines) and those of Hejazi *et al.* [26] (markers). It is evident that the two sets of results are in excellent agreement. The dispersion curves show that small wavelength perturbations seem to be unstable in all cases, with there is a distinct fastest growing mode. The figure clearly establishes that even if one of the interfaces, i.e., either the interface between A and C or that between B and C become unstable (as determined by their respective $R_{B|C}$ values), the entire front also becomes unstable as a result.

IV. RESULTS AND DISCUSSION

In what follows, we shall mainly focus on the impact of hydrodynamic dispersion and diffusivity contrast on the VF instabilities occurring at the reactive mixing interface. The extent of hydrodynamic dispersion is controlled by the dispersion lengths, i.e., η_L and η_T, while the diffusivity contrast is captured by the ratios Λ_i's. At the same time, the competition between dispersion and pure molecular diffusion also depends on Pe (recall that $\mathrm{Pe} = \mathrm{Da}$ here identically), and thus it is another important factor toward governing the stability of the front. Therefore, the focus will lie on assessing the impact of the parameters mentioned above on the ensuing stability of the reaction front.

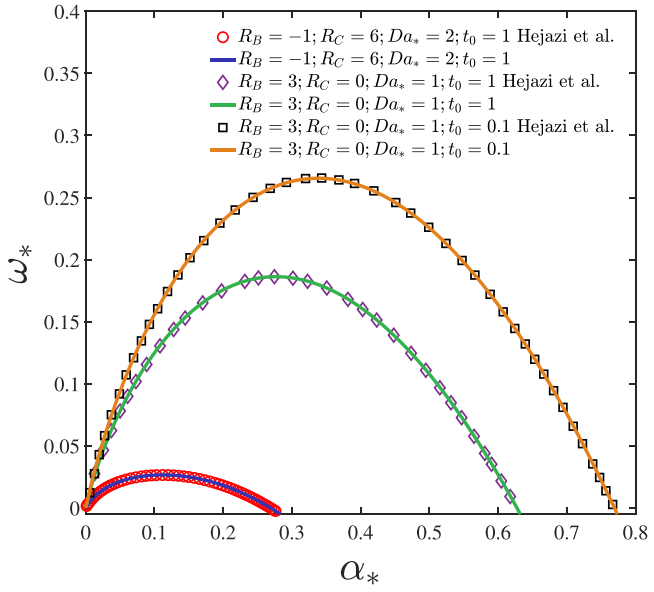

FIG. 2. Dispersion curves (ω_* vs α_*) showing the comparison of our quasisteady numerical results in the absence of hydrodynamic dispersion ($\eta_L = \eta_T = 0$, solid lines) with those of Hejazi *et al.* [26] (markers). Parameter values chosen are $\mathrm{Da}_* = 2$ and 1, $R_B = -1$ and 3, $R_C = 6$ and 0, at times $t_0 = 1$ and 0.1.

It is important to keep in mind that the viscosity contrasts between the various solutions also remain a key factor which influence the front's stability. These variations are encoded in the log ratios R_A, R_B, and R_C, and we have observed that primarily the differences between the log ratios, i.e., the signs and the magnitudes of the factors $R_B - R_A$ and $R_C - R_A$ (and thereby $R_B - R_C$) influence the growth of the perturbations. Hence, without loss of generality, we may assume $R_A = 0$, which helps us reduce the size of the relevant parameter space without sacrificing the essential physics. This essentially implies that the presence of species A does not impact of the viscosity of the solvent. Hejazi *et al.* [26] explored in detail the impact of various combinations of R_B and R_C (R_A was also dropped in their analysis) on VF instabilities. Therefore, for conciseness, in this article we shall focus on two types of viscosity profiles, chosen to best highlight the role played by hydrodynamic dispersion, and diffusivity contrast. These particular profiles are shown in Fig. 3. The first scenario [Fig. 3(a)] corresponds to $\mu_B > \mu_C > \mu_A$ ($=\mu_s$), which entails $R_B > R_C > 0$. We refer to this scenario as the monotonically increasing viscosity profile, wherein the viscosity continually increases from left to right. This corresponds to the situation where less viscous fluids try to displace fluids with larger viscosity, and is thus unstable from the very beginning. As the reaction progresses, the product C accumulates within the front. Since its viscosity is lower than that of B and higher than that of A, both the trailing interface (where A displaces C) and the leading interface (where C displaces B) of the reaction front continue to be unstable because of the unfavorable local viscosity contrast. Therefore, under the monotonic nature of the viscosity profile, both interfaces are expected to contribute to the overall instability, making this scenario particularly favorable for the growth of perturbations.

The second scenario [Fig. 3(b)] corresponds to $\mu_B < \mu_A$ and $\mu_C > \mu_A$, and thus $R_B < 0$, and $R_C > 0$ [26]. We refer to this as the mixed viscosity profile, wherein the interface is initially stable because $R_B < 0$. However, the formation of a highly viscous product C creates a destabilizing effect, particularly near the trailing edge of the reaction front where A displaces C. The leading edge, however, is expected to remain stable because $R_B < R_C$.

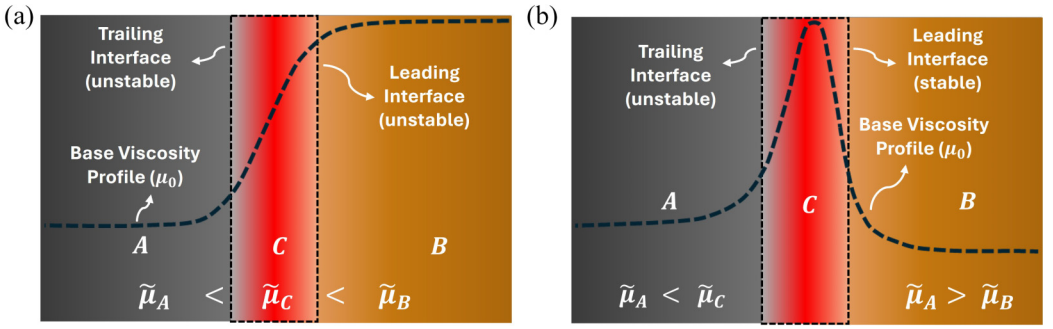

FIG. 3. Schematic diagrams of the reaction front showing the viscosity profiles for (a) monotonically increasing scenario ($\mu_A < \mu_C < \mu_B$) and (b) the mixed scenario ($\mu_A < \mu_C$, and $\mu_A > \mu_B$). The black dashed curves in both panels represent the base viscosity profile $\mu_0(x, t)$. The stable and unstable faces of the reaction fronts have also been indicated in each panel.

A. Impact of hydrodynamic dispersion on viscous fingering instabilities

1. Monotonically increasing viscosity profile ($\mu_A < \mu_C < \mu_B$)

We begin by comparing the growth rates obtained using the IVP approach with those from the QSSA for a monotonic viscosity profile. Figure 4 presents the variations in the growth rate (ω) vs t for multiple values of wave number $\alpha = 0.2,$ and 0.4, for the case of pure longitudinal dispersion with $\eta_L = 1$ in Fig. 4(a), and for the case of pure transverse dispersion with $\eta_T = 1$ in Fig. 4(c). Figures 4(b) and 4(d), respectively, show ω vs t curves for various choices of $\eta_L = 1$ and 2,

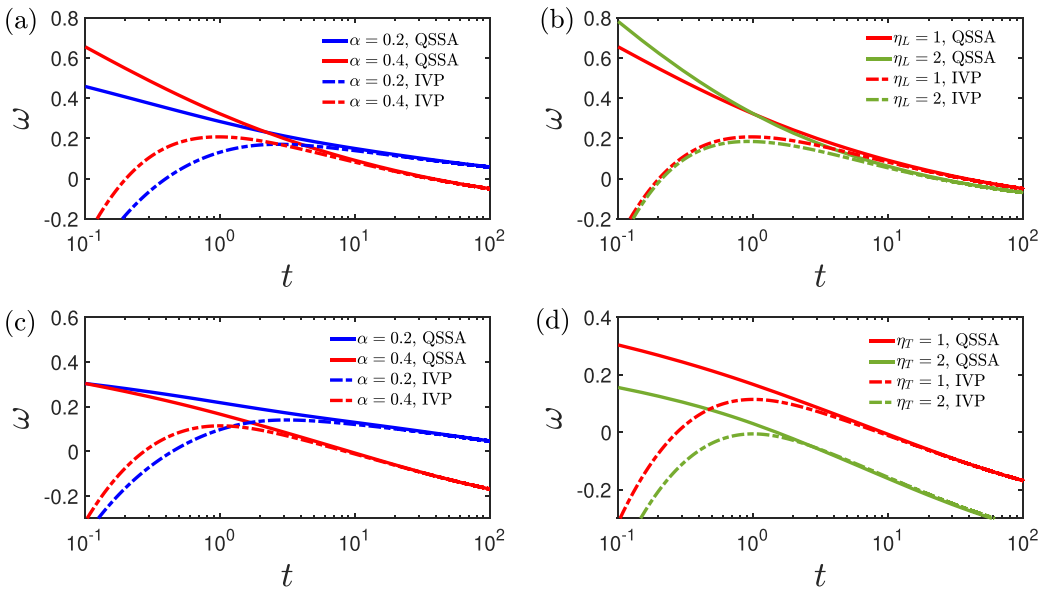

FIG. 4. Growth rate (ω) vs t for multiple values of wave number $\alpha = 0.2,$ and 0.4 in case of pure longitudinal dispersion with $\eta_L = 1$ in (a) and pure transverse dispersion with $\eta_T = 1$ in (c). Plot of ω vs t for $\eta_L = 1,$ and 2 in (b) and for $\eta_T = 1,$ and 2 in (d), with $\alpha = 0.4$ fixed in both panels. The QSSA (solid lines) and IVP approach (dashed-dotted lines) based results are compared here. Other parameter values are $R_B = 5,\ R_C = 2,\ \Lambda_B = \Lambda_C = \mathrm{Pe} = 1.$

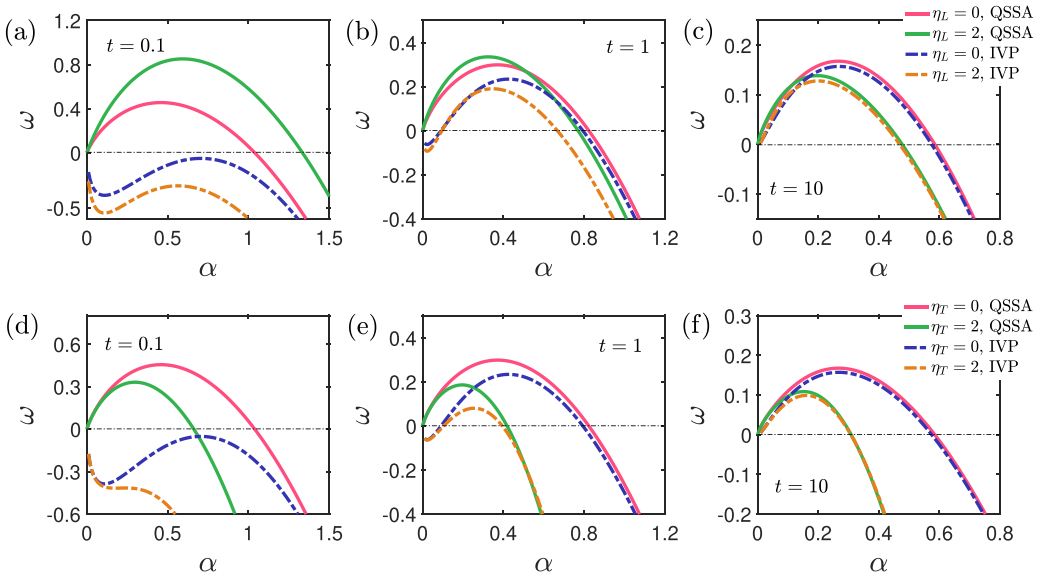

FIG. 5. Dispersion curves (ω vs α) for (a)–(c) pure longitudinal dispersion with varying $\eta_L = 0$ and 2, respectively, at times $t = 0.1$, 1, and 10. (d)–(f) ω vs α for pure transverse dispersion with varying $\eta_T = 0$ and 2, respectively, at times $t = 0.1$, 1, and 10. Both IVP (dashed-dotted) and QSSA (solid) results are shown. Other parameter values are $R_B = 5$, $R_C = 2$, $\Lambda_B = \Lambda_C = \mathrm{Pe} = 1$.

and $\eta_T = 1$ and 2 with the wave number held fixed at $\alpha = 0.4$. Solid lines represent the QSSA predictions, whereas dashed-dotted lines correspond to the IVP results. Other parameter values are mentioned in the caption.

It is evident from Fig. 4 that a clear difference between the two approaches (QSSA and IVP) exist at early times, with the QSSA consistently overpredicting the growth rates relative to the IVP approach. However, at later times ($t \sim 10$), the growth rates obtained from the two approaches converge across all cases considered. Indeed, similar trends have been reported earlier [63], while the results here also establish the accuracy of the growth rates computed using the IVP approach. Several other noteworthy observations may also be made. For instance, Fig. 4(b) shows that increasing the longitudinal dispersion coefficient (η_L) enhances the growth rates at early times according to the QSSA with a crossover occurring at $t \sim 1$. However, this trend reverses when the IVP approach is used, as a relatively larger η_L always leads to smaller ω values. On the other hand, Fig. 4(d) reveals that increasing the transverse dispersion coefficient (η_T) suppresses the growth rates at all times, according to both the IVP approach as well as the QSSA.

Figure 5 exhibits the dispersion curves (ω vs α) to further unveil the influence of pure longitudinal and transverse dispersion on the stability of the reaction front. Figures 5(a)–5(c) show the dispersion curves for various choices of η_L, respectively, at times $t = 0.1$, 1, and 10, while Figs. 5(d)–5(f) display the corresponding curves for various choices of η_T at those same time instances. Results computed from both the IVP approach (dashed-dotted lines) and the QSSA (solid lines) have been plotted in all panels. Values of all other relevant parameters are provided in the figure caption.

Akin to Fig. 4, Figs. 5(a), 5(b), 5(d), and 5(e) also show that the growth rates predicted by the QSSA and the IVP approach differ significantly across wave numbers at early times ($t = 0.1$ and 1). The relative influence of longitudinal dispersion also remains identical to Fig. 4; whereas QSSA predicts an increase in ω with η_L, the IVP approach yields the exact opposite trend essentially at all times [Fig. 5(a)]. The growth rates computed from the two methods show better agreement across wave numbers at time $t = 1$ [Figs. 5(b) and 5(e)], while they match very well at $t = 10$ and beyond

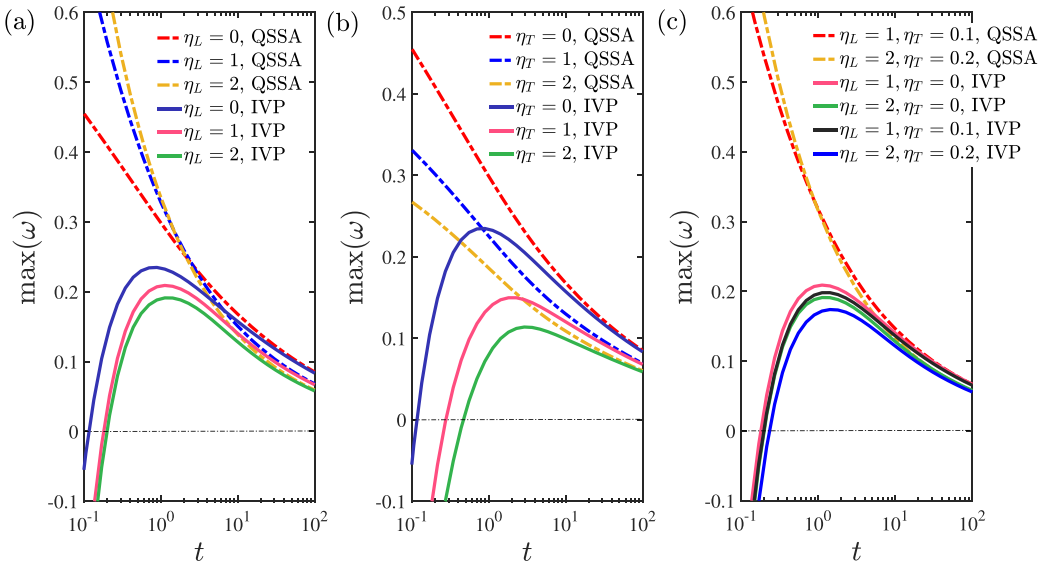

FIG. 6. Plot of maximum growth rate (max(ω)) vs t for (a) pure longitudinal dispersion with $\eta_L = 0,\ 1,$ and 2; (b) pure transverse dispersion with $\eta_T = 0,\ 1,$ and 2; and (c) anisotropic dispersion with $\eta_L = 1$ and 2 while $\eta_T = 0.1\eta_L$. In this panel, max(ω) for pure longitudinal dispersion ($\eta_L = 1$ and 2) has also been shown for comparison. Dashed-dotted lines are for QSSA and the solid lines are for IVP. Other parameter values are identical to those in Fig. 5.

[Figs. 5(c) and 5(f)]. At such later times, both QSSA and IVP approaches predict that longitudinal dispersion has a stabilizing influence on the reaction front. The apparent conundrum regarding the role of longitudinal dispersion at early times based on the two approaches have been resolved in the discussion ahead (see Fig. 6)—we argue that the IVP approach yields the correct trend in this regard. On the other hand, both approaches consistently predict that the presence of transverse dispersion [Figs 5(d)–5(f)] always suppresses the growth of perturbations, and this suppression is significantly stronger than that of pure longitudinal dispersion. Again, the reason behind this trend has been discussed in relation to Fig. 6—see ahead. Another interesting observation is that the ω values based on the two approaches (QSSA and IVP) tend to show relatively better agreement for small wavelength disturbances (large α), particularly at $t = 1$ and beyond. This is possibly because short wavelength disturbances always evolve relatively rapidly and thus satisfy the conditions required for the QSSA to a larger extent, leading to relatively better agreement.

Before trying to unpack the reasoning behind the variations in ω caused by η_L and η_T as shown in Fig. 5, it may be worth looking into the variations in ω over a long time period. To this end, in Fig. 6 we plot the maximum growth rate [max(ω), the peak growth rate at a given t across all wave numbers α] computed based on the IVP approach as a function of time (t) for the case of pure longitudinal dispersion in Fig. 6(a), pure transverse dispersion in Fig. 6(b), and for the general case of anisotropic dispersion in Fig. 6(c). The other parameter values remain identical to those in Fig. 5. For comparison, the QSSA results are also shown with dashed lines. Examining Figs. 6(a) and 6(b), it is evident that both longitudinal and transverse dispersion seem to have a stabilizing impact on the reaction front at all times, according to the IVP approach.

The impact of transverse dispersion is relatively straightforward to explain. It enhances mixing along the reactive front (i.e., perpendicular to the direction of flow), and therefore any fluctuations in the concentrations are quickly smeared out by transverse dispersion. This suppresses any subsequent increments in the viscosity contrast, and thus reduces the growth rate of the perturbations—see Figs. 5(d)–5(f) and Fig. 6(b). In contrast, the impact of longitudinal dispersion is governed by two

competing factors. On one hand, it enhances streamwise mixing and hence augments the reaction rate in the base flow itself (note that transverse dispersion has no impact on the base concentration). Figure 14 in Appendix B confirms that for a monotonically increasing viscosity profile, the reaction indeed tends to aid the instabilities in the presence of dispersion. Since longitudinal dispersion enhances the reaction rate, it may also be expected to amplify any streamwise fluctuations in concentrations and thereby the local viscosity gradients. On the other hand, it also causes enhanced mixing, which again naturally tends to smear out concentration (and viscosity) gradients. Thus, akin to transverse dispersion, longitudinal dispersion (η_L) is also expected to assert a stabilizing influence and help suppress the growth of the underlying disturbances. The results, however, indicate that the stabilizing influence of pure longitudinal dispersion associated with enhanced mixing dominates over the destabilizing effect arising from product formation, leading to an overall reduction in the values of ω with increasing η_L. However, because of its accompanying destabilizing influence, longitudinal dispersion reduces ω by a far smaller extent than the transverse one.

Figure 6(c) compares the maximum growth rate for pure longitudinal dispersion with that of anisotropic dispersion (both η_L and η_T are nonzero), wherein the value of η_L has been kept unchanged between the two scenarios. In most porous media of practical interest, the ratio of longitudinal to transverse dispersion coefficients is typically $O(10)$ [73]. This same ratio has been maintained in the panel under consideration. As a consequence, there is not much difference between the anisotropic and pure longitudinal dispersion scenarios as far as the variations in $\max(\omega)$ are concerned. Overall, Fig. 6(c) as well as the other panels in Fig. 6 establish that for a monotonically increasing viscosity profile ($R_B > R_C > 0$), the influence of both longitudinal and transverse dispersion weakens as time progresses, driven mainly by the weakening of the viscosity gradients because of mixing. In the rest of this section, all results pertain to the anisotropic dispersion scenario (unless otherwise mentioned) where $\eta_L > \eta_T$.

2. *Mixed viscosity profile ($\mu_C > \mu_A$, and $\mu_A > \mu_B$)*

A mixed (i.e., nonmonotonic) viscosity profile characterized by $\mu_A < \mu_C$, and $\mu_A > \mu_B$ [see Fig. 3(b)] presents another intriguing set of scenarios, wherein the reaction causes an inherently stable front to become unstable. Similar to the case of the monotonic viscosity profile (Fig. 5), we begin by comparing the dispersion curves (ω vs α) obtained using the IVP approach (dashed-dotted lines) with those predicted by the QSSA (solid lines) in Fig. 7. Figures 7(a)–7(c), respectively, show the dispersion curves for various choices of η_L at times $t = 1$, 10, and 100. Panels (d)-(f) display the corresponding results for various choices of η_T at those same time instances. Values of all other relevant parameters are provided in the figure caption.

Akin to Figs. 4–6, we observe clear differences between the IVP approach and the QSSA at $t = 1$ and 10 [see Figs. 7(a)–7(b) and 7(d)–7(e)]. When $t \geqslant 100$, the growth rates obtained using the two approaches coincide with each other (panels (c) and (f)). This indicates that in contrast to the case of a monotonic viscosity profile, the convergence between QSSA and IVP is achieved at a much later time for a mixed viscosity profile. This is because the mixed-viscosity profile is originally stable in the absence of chemical reaction. The formation of the product gradually destabilizes the trailing edge by making the viscosity profile more favorable to viscous fingering. Consequently, the perturbations actually decay at early times [see Figs. 7(a)–7(b) and 7(d)–7(e)], regardless of the choice of η_L and η_T. They only start to grow once sufficient amount of product has formed to turn the viscosity profile susceptible to fingering instability, which occurs when $t \sim O(10) - O(10^2)$. The QSSA on the other hand inaccurately suggests that the front becomes unstable right from the onset, which delays the convergence between the QSSA and the IVP method.

Figure 8 displays the maximum growth rate [$\max(\omega)$] as a function of time (t) for various choices of $\eta_L = 0.5,\ 1$, and 2 with $\eta_T = 0.1$ fixed in Fig. 8(a) and for various choices of $\eta_T = 0.1,\ 0.2$, and 0.5 with $\eta_L = 1$ fixed in Fig. 8(b). The respective insets show the dispersion curves(ω vs α) obtained using the IVP approach (solid lines) and QSSA (dashed lines) at $t = 100$. This is a composite diagram; the results for $t < 100$ are taken from IVP analysis, and those for $t > 100$ are

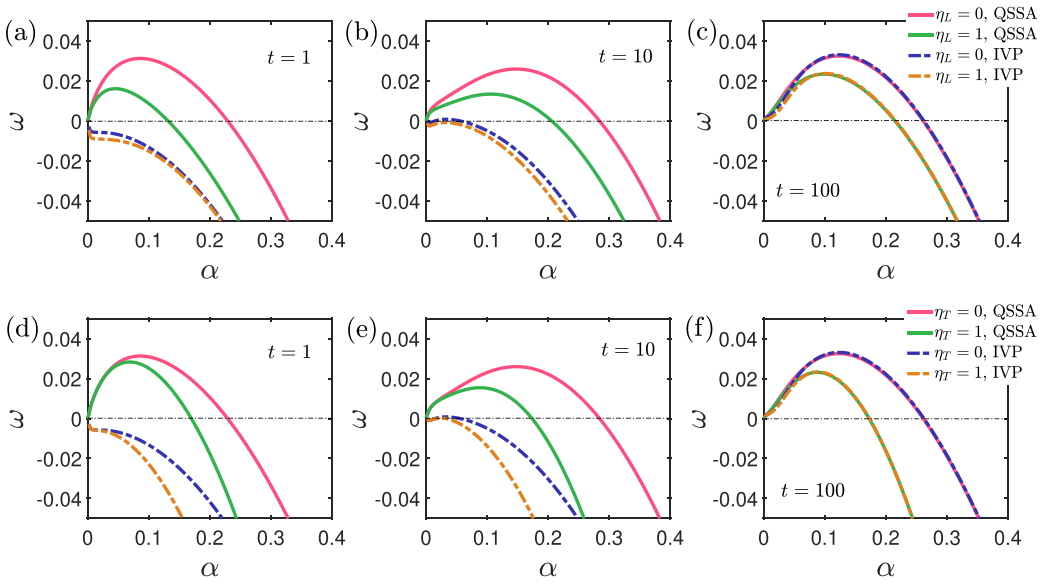

FIG. 7. Dispersion curves (ω vs α) computed based on the IVP approach (dashed-dotted lines) and the QSSA (solid lines), for pure longitudinal dispersion with $\eta_L = 0$ and 1 in (a)–(c), and for pure transverse dispersion with $\eta_T = 0$ and 1 in (d)–(f). Each panel represents the dispersion curves at a specific time as follows: (a), (d) $t = 1$; (b), (e) $t = 10$; (c), (f) $t = 100$. Other parameter values are $R_B = -2,\ R_C = 5,\ \Lambda_B = \Lambda_C = \mathrm{Pe} = 1$.

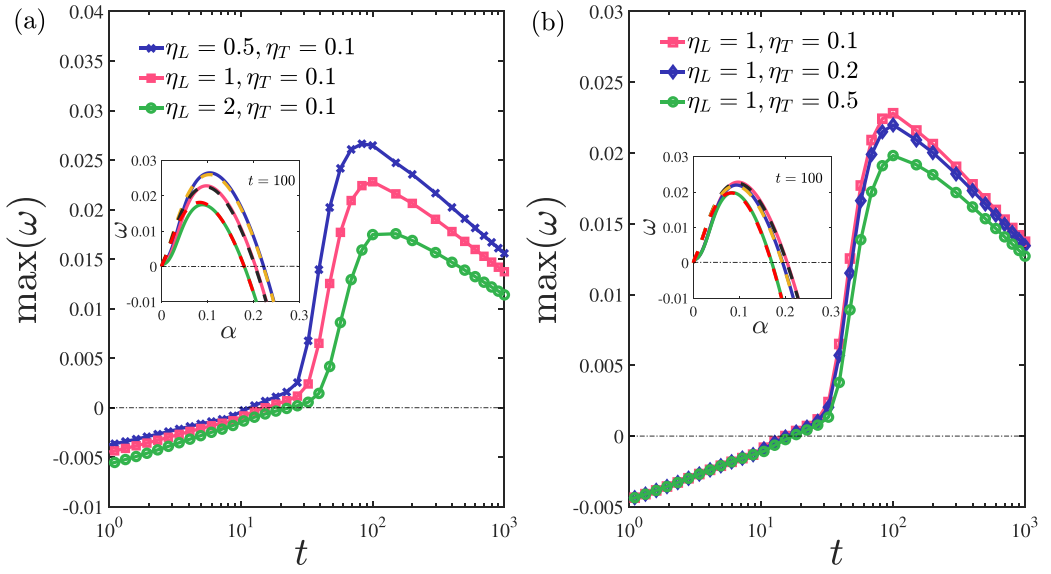

FIG. 8. Composite plot of $\max(\omega)$ vs t with IVP approach based results till $t = 100$ and QSSA afterward for various choices of (a) $\eta_L = 0.5,\ 1,\ 2$ with fixed $\eta_T = 0.1$ and (b) $\eta_T = 0.1,\ 0.2,\ 0.5$ with fixed $\eta_L = 1$. The respective insets show the dispersion curves obtained using the IVP approach (solid lines) and the QSSA (dashed lines) at $t = 100$ for the same parameter values as in the main panel. Other parameters are taken as $R_B = -2,\ R_C = 5$ (mixed profile), $\Lambda_B = 1,\ \Lambda_C = 1,\ \mathrm{Pe} = 1$.

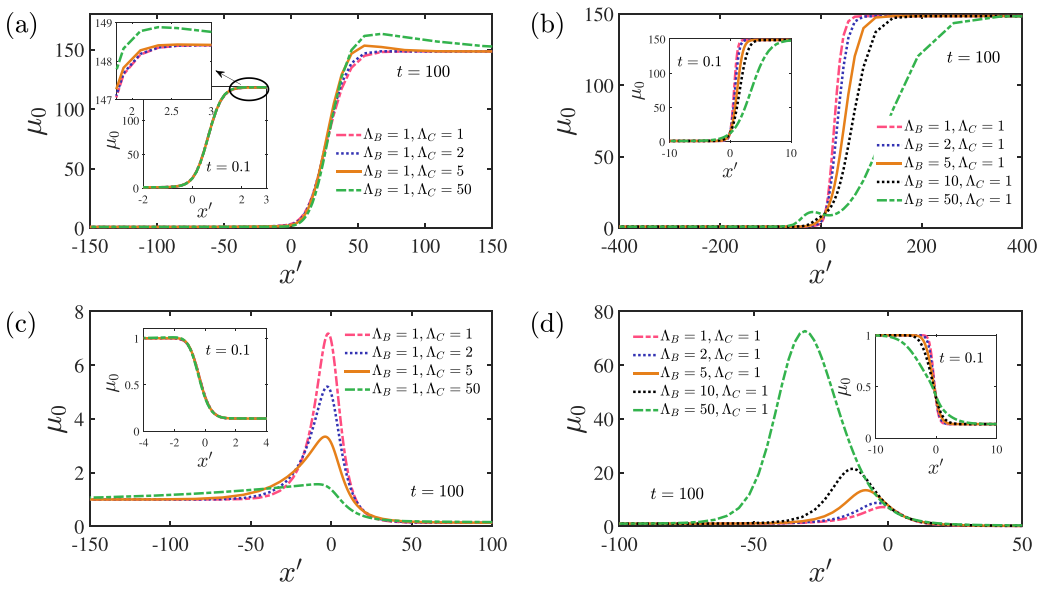

FIG. 9. Base viscosity profile (μ_0) at $t = 100$ for (a), (c) various choices of $\Lambda_C = 1,\ 2,\ 5,\ 50$ with $\Lambda_B = 1$ and (b), (d) various choices of $\Lambda_B = 1,\ 2, 5,\ 10,\ 50$ with $\Lambda_C = 1$. Panels (a), (b) are for monotonic viscosity profile with $R_B = 5$ and $R_C = 2$. (c), (d) Corresponding results for a mixed viscosity profile with $R_B = -2$ and $R_C = 5$. The respective insets show the corresponding base viscosity profiles at $t = 0.1$. Values of other relevant parameters are $\mathrm{Pe} = 1,\ \eta_L = 1,\ \eta_T = 0.1$.

based on QSSA, because by $t \sim 100$ the two approaches yield the same growth rates (see the insets), while QSSA is computationally far less taxing than IVP. Values of all other relevant parameters are mentioned in the caption.

This figure vividly shows that for a mixed viscosity profile, the front initially stays stable, while the onset of instability occurs beyond a critical time at around $t \sim 20$, such that the reaction has sufficient time to progress. This is in direct contrast to the results of QSSA [26], which predict instability right from $t = 0$. The reduction in $\max(\omega)$ beyond $t \sim 100$ likely stems from enhanced mixing and a slowdown in the production of C at the front, leading to a relatively smaller viscosity gradient which has a stabilizing influence. Similar to the case of monotonic viscosity profile explored in Sec. IV A 1, both longitudinal (η_L) and transverse (η_T) dispersion tend to suppress the growth of the instabilities essentially at all times. Hydrodynamic dispersion (both longitudinal and transverse) clearly seems to enhance mixing and smear out concentration fluctuations, which results in such a stabilizing influence. Finally, for a mixed viscosity profile, one side of the mixing front (the leading edge) becomes stable, and this leads to a drastic reduction in the growth rate of the perturbations—compare the values of $\max(\omega)$ in this figure and those in Fig. 6.

B. Impact of diffusivity contrast

The molecular diffusivity of various chemically reactive species in the subsurface are generally different from each other, and this mismatch can play a critical role in governing the evolution of the perturbations [56,74,75]. In an effort to resolve the impact of diffusivity contrast between the reactants and the product, we begin by probing how they influence the variations in viscosity across the front, because it is the viscosity profile that triggers the subsequent instabilities. We recall that there are two distinct scenarios in this regard: a monotonically varying viscosity profile ($R_B > R_C > 0$) and a mixed viscosity profile ($R_C > 0$ and $R_B < 0$). Figure 9 plots the base viscosity (μ_0) as a function of x' for various choices of diffusivity ratios (denoted by Λ_B and Λ_C; by default

$\Lambda_A = 1$) in the scenarios mentioned above. Figures 9(a) and 9(b) show the μ_0 vs x' curves for a monotonically increasing viscosity profile ($R_B = 5$ and $R_C = 2$) at $t = 100$, and various choices of Λ_C and Λ_B respectively. Figures 9(c) and 9(d) show the corresponding results for a mixed viscosity profile ($R_B = -2$ and $R_C = 5$). The insets in all panels exhibit the base viscosity profiles at $t = 0.1$, with other parameters remaining identical to the respective main figures. The values of all other relevant parameters are listed in the figure caption.

For a monotonically increasing viscosity profile [Fig. 9(a)], the diffusivity of the product seems to have relatively little impact on the variability in the base viscosity. It is, however, interesting to note that μ_0 exhibits a nonmonotonic variation with a peak just downstream of the front, when Λ_C is relatively large [$\geqslant 5$; see the yellow and the green curves in Fig. 9(a)]. In this scenario, the rise in μ_0 becomes relatively sharper, while the subsequent fall in its value occurs gradually. The reason for such variations may be attributed to the high diffusivity of the product, which helps it quickly penetrate deep into the region occupied by the reactant B. A steeper ascent in μ_0 is expected to facilitate the growth of the disturbances, while the subsequent fall in its value should have a stabilizing influence. Therefore, in the scenario $R_B > R_C > 0$, increasing the product's diffusivity seems to have both stabilizing and destabilizing roles, with the stabilizing influence being perhaps a little weaker owing to the small accompanying viscosity gradients. These two effects are expected to largely cancel each other and thus the product's diffusivity should not have a strong impact on the stability of the front in case of a monotonically increasing viscosity profile.

On the other hand, for a mixed viscosity profile [Fig. 9(c)], increasing Λ_C evidently smoothens out any viscosity contrast across the reaction front, although at small times, this effect is negligibly small [inset in Fig. 9(c)]. Any reduction in the viscosity contrast would naturally have a stabilizing influence on the front, and thus for the case of mixed profile, enhanced product diffusivity should suppress the growth of the perturbations, and perhaps may even completely stabilize the front (as we show shortly).

Increasing the diffusivity of the reactant B (i.e., Λ_B) is expected to enhance mixing across the front, thus resulting in an augmented reaction rate. For a monotonically increasing viscosity profile [Fig. 9(b) and its inset], this naturally leads to a more gradual increase in μ_0 with x', and therefore reduces the intensity of the viscosity contrast that drives the instabilities. As a consequence, one would expect a relatively larger reactant diffusivity to help suppress the growth of the perturbations around the front. However, this same enhanced diffusivity should also lead to increased product formation, and hence for a mixed viscosity profile [Fig. 9(d)], the extent of the viscosity's variability across the front will increase with Λ_B. Recalling that for mixed viscosity, the instabilities are instigated by the formation of the product (and the viscosity contrast resulting from it), one expects Λ_B to have a largely destabilizing impact in such scenarios, especially at larger times. The inset of [Fig. 9(d)], however, shows that at early times, the viscosity profile remains monotonic regardless of the choice of Λ_B, although increasing its value decreases the spatial gradient of μ_0. Since the initial ($t = 0$) viscosity profile ($\mu_A > \mu_B$) is actually stable, a sharp change from μ_A to μ_B will favor stability, while a more gradual change will tend to push the front toward instability. Therefore, it follows that at early times one should also expect Λ_B to have a destabilizing influence on the front, especially when it is sufficiently large.

We now set out to test the series of predictions made based on Fig. 9 regarding the influence of Λ_B and Λ_C on the stability characteristics of the reaction front. To this end, Fig. 10 shows the temporal (t) evolution of maximum growth rate ($\max(\omega)$) for various choices of Λ_C in panel (a) and those of Λ_B in panel (b), when the viscosity increases monotonically ($\mu_A < \mu_C < \mu_B$ or, $R_B > R_C > 0$). The respective insets show the dispersion curves for the same parameter values at $t = 20$. All data points in both panels have been computed using the IVP approach. Values of other relevant parameters are mentioned in the caption. Referring back to Fig. 9(a), it was noted that for a monotonically increasing viscosity profile, Λ_C (diffusivity of the product) is expected to have negligible impact on the stability of the front. This is exactly what is observed in Fig. 9(a) here, where $\max(\omega)$ changes only by a small amount upon increasing Λ_C 50-fold. The small increase noted in $\max(\omega)$ at later

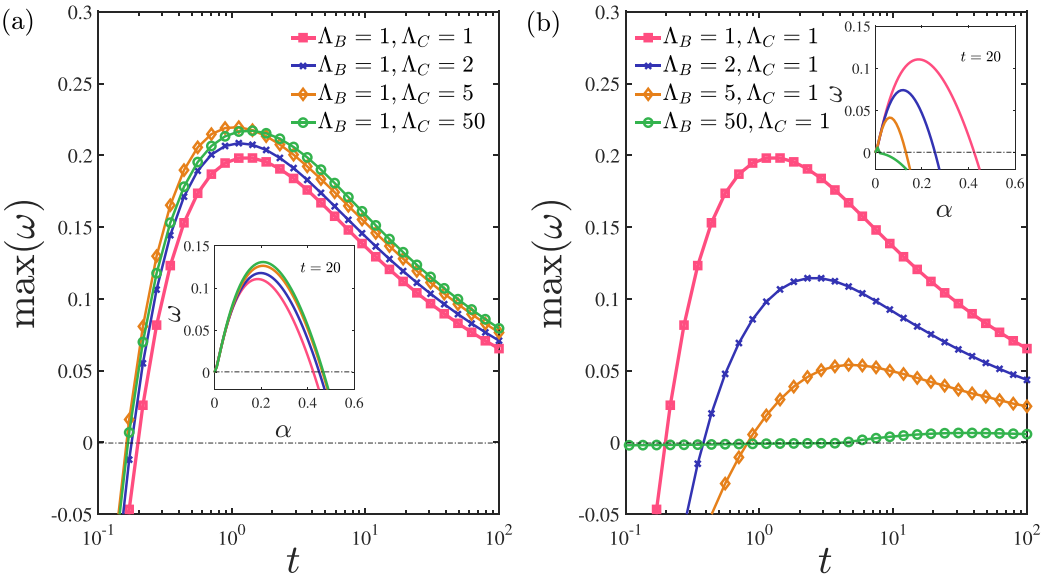

FIG. 10. Maximum growth rate [max(ω)] versus time (t) for (a) various choices of $\Lambda_C = 1,\ 2,\ 5$, and 50 with $\Lambda_B = 1$ and (b) various choices of $\Lambda_B = 1,\ 2,\ 5$, and 50 with $\Lambda_C = 1$. The respective insets show the dispersion curves at time $t = 20$. Other parameter values are $R_B = 5,\ R_C = 2,$ (monotonic profile) Pe $= 1,\ \eta_L = 1$, and $\eta_T = 0.1$. All results are based on the IVP approach.

times may be attributed to the relatively weak (descending) gradient in μ_0 ahead of the peak shown in Fig. 9(a), as compared to a far steeper increase in μ_0 near the trailing edge of the reaction front. On the other hand, in the discussion related to Fig. 9(b), it was noted that any enhancement in the diffusivity of the reactant should reduce the growth of the perturbations, owing to the diminishing viscosity gradients across the front. Indeed, this is exactly what is observed in Fig. 9(b) here, where increments in Λ_B seem to diminish max(ω) to a significant extent. Furthermore, the inset in this panel also demonstrates that the range of unstable wave numbers shrink upon increasing Λ_B, further denting the instabilities at the front.

Figure 11 showcases the temporal evolution of max(ω) as a composite plot constructed using both IVP analysis and QSSA (IVP results taken till $t = 500$) for various choices of Λ_C in Fig. 11(a), and those of Λ_B in Fig. 11(b) for a mixed viscosity configuration ($R_B < 0$ and $R_C > 0$). The insets in each panel depict the dispersion curves for the same set of parameters as in the main figures. Values of all other relevant parameters are mentioned in the figure caption. Recall that Fig. 9(c) suggests that, for a mixed viscosity profile, any increments in Λ_C (product's diffusivity) should reduce the growth rate of the perturbations by smearing out the viscosity gradients from which the instabilities emerge. Figure 11(a) here perfectly agrees with this prediction. Furthermore, upon increasing Λ_C, the range of unstable wave numbers also diminish significantly. In fact, as speculated while discussing Fig. 9(c) earlier, all disturbances become stable when $\Lambda_C = 40$, which results in max(ω) < 0 for all times, and hence a complete stabilization of the front. This constitutes an example of how molecular diffusivity contrasts between the product and the reactants may turn an unstable front into a stable one.

Figure 11(b) also agrees with the assessments made based on Fig. 9(d). At early times and also at later times, enhancements in Λ_B indeed cause the maximum growth rate to rise, thus making the front increasingly unstable. For $\Lambda_B = 40$, max(ω) exhibits oscillatory behavior, indicating that for mixed viscosity profiles with extremely large diffusivity contrasts, the peak growth rates may shuttle between extreme values. These oscillations likely emerge from the dual role (i.e., both stabilizing and destabilizing) of Λ_B; see the discussion related to Fig. 9(d). Figures 10 and 11 thus establish

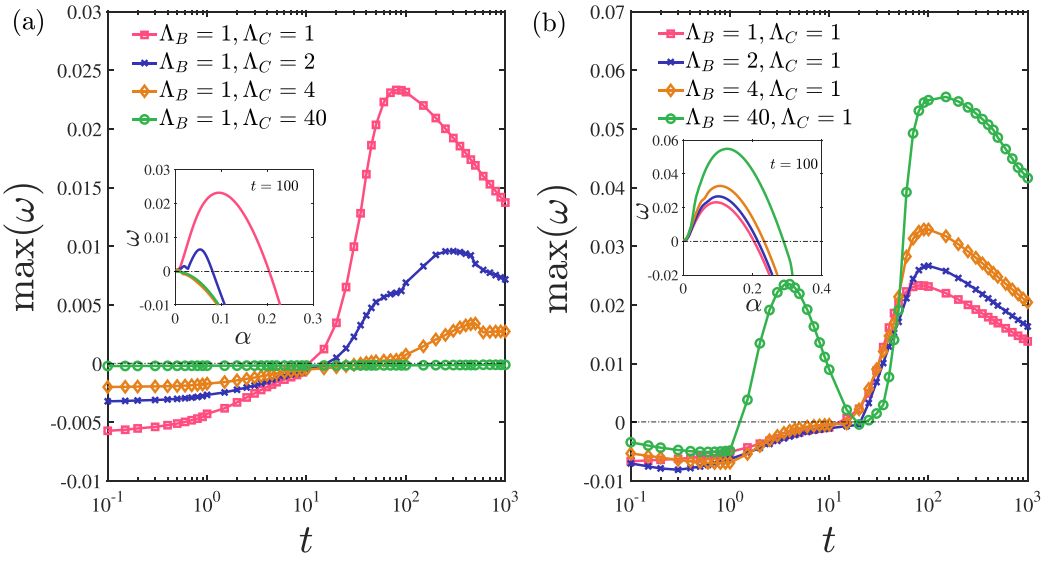

FIG. 11. Maximum growth rate [max(ω)] versus time (t) for (a) various choices of $\Lambda_C = 1,\ 2,\ 4$, and 40 with $\Lambda_B = 1$ and (b) various choices of $\Lambda_B = 1,\ 2,\ 4$, and 40 with $\Lambda_C = 1$. The respective insets show the dispersion curves at time $t = 100$. Other relevant parameter values are $R_B = -2,\ R_C = 5$ (mixed profile), Pe $= 1,\ \eta_L = 1$, and $\eta_T = 0.1$. This is a composite plot with IVP results taken till $t = 500$ and QSSA afterward.

that the stability characteristics of a reaction front may indeed depend strongly on the diffusivity contrasts between the product and the reactants, and are largely controlled by the impact of the latter on the base viscosity profile.

In view of the qualitative shift in the stability characteristics observed especially in Fig. 11(a), it is tempting to have a closer look at the growth rate across a large span of Λ_C and Λ_B values. This is done in Fig. 12, where the contours of max(ω) in the $\Lambda_C - t$ plane [Fig. 12(a)] and in the $\Lambda_B - t$ plane [Fig. 12(b)] are plotted in a composite phase diagram (results based on IVP approach till

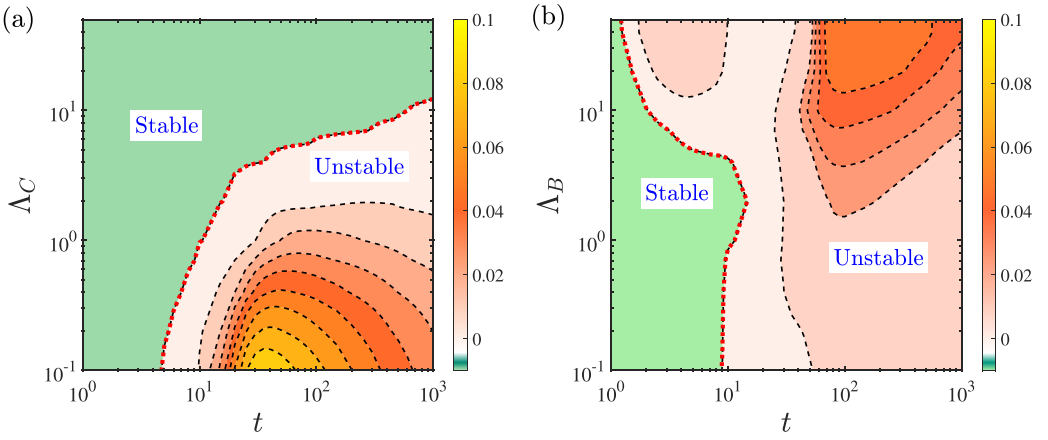

FIG. 12. Composite contour plot (IVP approach till $t = 500$, and QSSA afterward) of max(ω) on (a) the $\Lambda_C - t$ plane and (b) the $\Lambda_B - t$ plane for the mixed viscosity profile with $R_B = -2$, and $R_C = 5$. The values of other relevant parameters are Pe $= 1,\ \eta_L = 1,\ \eta_T = 0.1$. The dotted red curves in (a) and (b) separate stable regions from the unstable ones.

$t = 500$, and QSSA beyond that), with other parameters remaining identical to Fig. 11. Figure 12(a) clearly shows that enhanced diffusivity of the product tends to reduce $\max(\omega)$ and eventually completely suppresses the instabilities by turning $\max(\omega)$ negative. The stable [$\max(\omega) < 0$, green] and unstable [$\max(\omega) > 0$] regions have been separated by a red dotted curve in both panels. It is evident from Fig. 12(a) that a sufficiently large Λ_C essentially makes the front completely stable, when the viscosity profile is mixed in nature. On the other hand, Fig. 12(b) establishes that the reactant's diffusivity (Λ_B) tends to facilitate instabilities especially at larger times, as also observed in Fig. 11(b). Furthermore, the extent of oscillations in $\max(\omega)$ with t also increases with increments in Λ_B, again in agreement with Fig. 11(b).

It is important to note that the instability mechanism here remains fundamentally viscosity controlled. Others, such as Mishra *et al.* [56] discuss another possible mechanism driven by double-diffusive viscous fingering (DD-VF), leading to instability, wherein diffusivity contrast as discussed above plays a key role. They establish that even in nonreactive systems, and in mixing fronts with strictly monotonic stable viscosity profile, the diffusivity-contrast between the various dissolved species may lead to destabilization and the formation of smooth finger patterns. Furthermore, such diffusivity contrasts may also trigger the formation of pockets of nonmonotonic viscosity variations near an originally stable mixing front,and subsequently destabilize it. However, such distinct purely double-diffusive instability mechanisms are not observed within the linear stability regime considered in our study.

C. Impact of Péclet number

We end our discussion by probing the impact of Péclet number (Pe) on the stability of the reaction front. Since Da (Damkölhler number) and Pe are identical in our analysis, their impact on the growth of the perturbations will also be identical to each other. Figure 13 presents the contours of the maximum growth rates [$\max(\omega)$] in the Pe $- t$ plane. Figures 13(a) and 13(b), respectively, show the contours for pure molecular diffusion ($\eta_L = \eta_T = 0$) and anisotropic dispersion ($\eta_L = 1,\ \eta_T = 0.1$), when the viscosity profile is monotonically increasing [$R_B = 5$ and $R_C = 2$, see Fig. 3(a)]. Figures 13(c) and 13(d) show the corresponding results for a mixed viscosity profile with $R_B = -2,$ and $R_C = 5$. All panels here depict composite phase diagrams with early time results ($t \leqslant 100$) taken from IVP analysis and the long time results computed using the QSSA. Values of other relevant parameters are specified in the figure caption. The corresponding dispersion curves are shown in Fig. 15 in Appendix C.

Figure 13(a) shows that in the absence of dispersion, the maximum growth rate continually increases with Pe, and this is particularly prominent at relatively early times, consistent with Fig. 6. Any increments in Pe starting from a small magnitude imply weakening diffusion, which reduces mixing and therefore destabilizes the reaction front when the viscosity profile is monotonically increasing. On the other hand, when dispersion is present [Fig. 13(b)], the maximum growth rate of the perturbations become independent of Pe (indicated by the nearly vertical contour lines) when Pe becomes sufficiently large. The reason for this becomes apparent upon examining the linear stability equations, i.e., Eqs. (13) [or Eqs. (16)]. Based on these, it is evident that the evolution of the perturbations become independent of Pe when Pe $\gg 1$ simply because terms like $\Lambda_{A|B|C}/\mathrm{Pe}$ may now be dropped, and this explains why the maximum growth should not depend on Pe. Physically, this implies that at sufficiently large Pe, mixing at the reaction front is mostly driven by dispersion (i.e., mechanical dispersion) which is independent of Pe, while molecular diffusion with which Pe is associated plays a negligible role in governing the base state as well as the perturbations. On the contrary, when dispersion is absent ($\eta_T = \eta_L = 0$), the diffusion term can not be trivially dropped from Eqs. (13) even if Pe $\gg 1$, as this alludes to a singular limit. In other words, no matter how large Pe becomes, in the case of pure molecular diffusion, it will always have an impact on the mixing at the front because it becomes the only mixing mechanism in such cases. One also notes that for Pe $\sim O(1)$, $\max(\omega)$ varies nonmonotonically with time, again consistent with the earlier observations in Fig. 6. In contrast, for sufficiently large Pe, $\max(\omega)$ decreases monotonically with

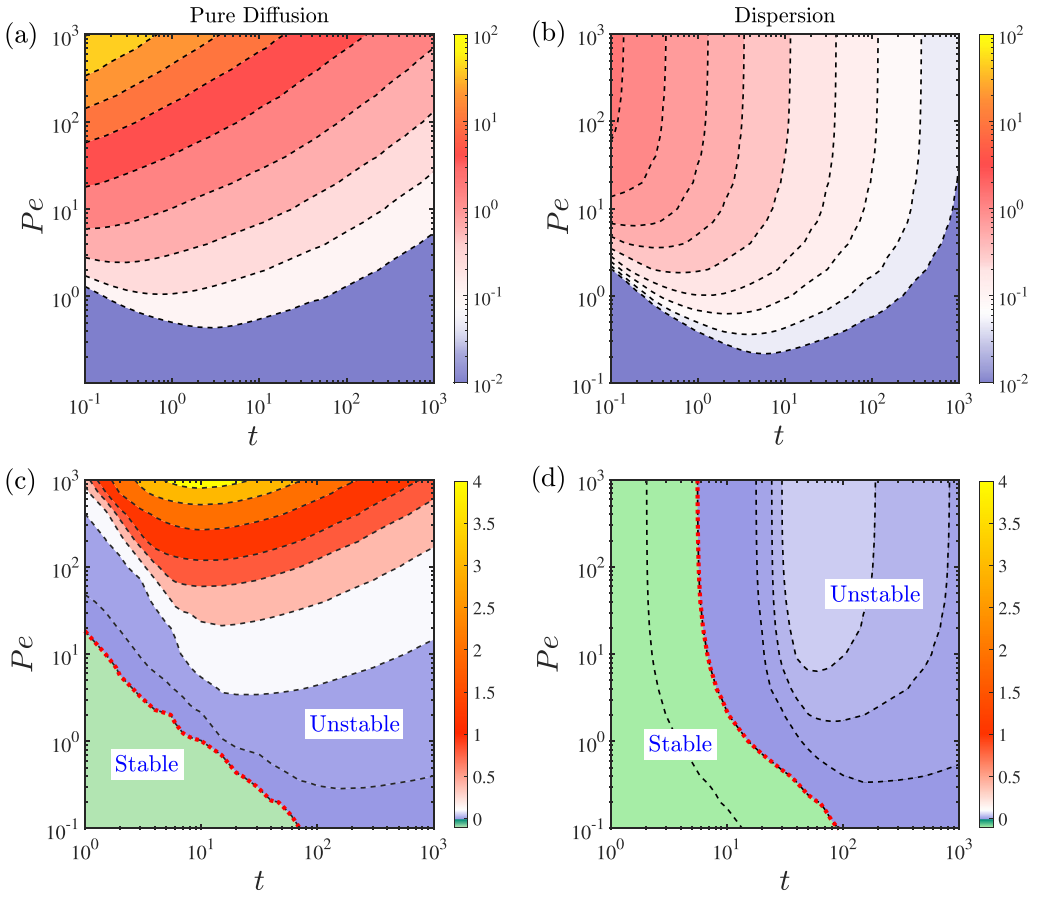

FIG. 13. Composite contour plot (IVP results taken till $t = 100$, and QSSA beyond that) of $\max(\omega)$ on the $\mathrm{Pe} - t$ plane for (a), (c) pure diffusion ($\eta_L = \eta_T = 0$) and (b), (d) anisotropic dispersion with $\eta_L = 1$, and $\eta_T = 0.1$. (a), (b) Monotonic viscosity profile with $R_B = 5$, and $R_C = 2$; (c), (d) corresponding results for a mixed viscosity profile with $R_B = -2$, and $R_C = 5$.Values of other relevant parameters are $\Lambda_B = \Lambda_C = 1$.

time, which agrees with the predictions of the QSSA also shown in Fig. 6. This is because at large Pe, perturbations undergo rapid amplification, and thus any changes in the base state have relatively little impact on their evolution, whilst the conditions also become more amenable to the application of QSSA.

Figure 13(c) reveals that Pe again has a largely destabilizing influence in the absence of dispersion ($\eta_L = \eta_T = 0$) when the front has a mixed viscosity profile ($\mu_A > \mu_B$ and $\mu_A < \mu_C$). However, now the growth rates are far weaker than those of a monotonic viscosity profile, while $\max(\omega)$ exhibits nonmonotonic behavior in time (t), essentially across all Pe—this is consistent with Fig. 11. In this scenario, the formation of the product is essential for instability, and hence the perturbations are expected to grow only when a sufficient amount of product has formed, which takes a certain amount of time [$\sim O(1)$]. Consequently, the instability sets in only after a critical time [shown by the red dotted line in panel Fig. 13(c)], which decreases with Pe; prior to this, the front remains stable (the green region). This is also why the maximum growth rate is observed [Fig. 13(c)] at intermediate times ($t \gtrsim 10$), unlike the case of monotonic viscosity profile where $\max(\omega)$ is at its peak at early times.

Figure 13(d), on the other hand, clearly establishes that dispersion has a strong stabilizing impact on the reaction front when the viscosity has a mixed profile—this is again in agreement with the

discussion in Sec. IV A 2. The nonmonotonic nature of $\max(\omega)$ still persists, albeit with a far lower intensity. Further, the instability again sets in only after a critical time, and unlike the case of pure diffusion {panel (c)}, this onset time now becomes independent of Pe when it is sufficiently large [see the red dotted line in 13(d)]. Akin to Fig. 13(b), the maximum growth rate also becomes independent of Pe when $\mathrm{Pe} \gg 1$ (indicated by the nearly vertical contour lines for large Pe values). Needless to state, such behavior stems from mechanical dispersion dominating the mixing process over molecular diffusion for large values of Pe, which negates Pe's influence on the base state as well as the perturbations. Perhaps the most important highlight of Fig. 13 is the qualitative changes in the contour plots of the growth rate which occur in the presence of dispersion, thus underlining its importance in reactive mixing processes.

V. CONCLUSIONS

In this article, we investigate the influence of hydrodynamic dispersion on the stability of a bimolecular reaction front. The local viscosity of the solution is taken to be a function of the concentrations of the reactants and the product and, therefore, the viscosity will evolve as the reaction progresses. The spatial variation of viscosity (e.g., when a less viscous fluid penetrates into a more viscous one) determines the stability of the front with regard to viscous fingering. We construct a Darcy-scale framework, wherein hydrodynamic dispersion becomes an integral part and is modeled as a second rank tensor linearly dependent on the Darcy-scale velocity. In addition, the reactants and the products are also assumed to have distinct molecular diffusivities. The stability of the reaction front is analyzed using two pathways: (i) a transient analysis based initial value problem (IVP) approach and (ii) a quasi-steady-state approximation (QSSA). The QSSA framework assumes that the base-state concentrations evolve slowly compared to the perturbations and performs the stability analysis by freezing the base state. In contrast, the IVP approach explicitly accounts for the temporal evolution of the unsteady base state and thus computes the transient growth rate by solving an initial value problem for a given mode. The resulting linearized problem is solved numerically using a combination of implicit finite difference and the Chebyshev spectral collocation method. Two representative viscosity profiles are examined: (i) a monotonically increasing profile ($\mu_A < \mu_C < \mu_B$ or, $R_B > R_C > 0$) from left to right and (ii) a mixed profile ($\mu_A < \mu_C$ and $\mu_A > \mu_B$, implying $R_B < 0,\ R_C > 0$), where the product is the most viscous. The former of these two profiles is inherently unstable to viscous fingering and the reaction makes it even more unstable. The latter (mixed profile) is inherently stable, and it is the reaction that instigates the growth of the perturbations.

Several important conclusions may be drawn from our results. First, we establish that the growth rates computed using the QSSA and the IVP approach differ significantly at early times, regardless of the choice of other parameters. However, at long time, when the conditions become conducive to QSSA, the values of ω deduced based on the two approaches converge exactly. The time taken for this convergence depends strongly on the viscosity profile. The two approaches converge relatively earlier for a monotonic viscosity profile than a mixed viscosity profile, simply because the former is inherently unstable and thus causes the perturbations to grow rapidly right from the onset. Second, we show that as per the IVP approach, both longitudinal and transverse dispersion tend to suppress the growth of the perturbations by facilitating mixing at all times, regardless of the viscosity profile. In contrast, the QSSA inaccurately predicts that longitudinal dispersion may destabilize a front at early times in case of monotonic viscosity profile, although at later times its prediction agrees with the IVP approach. Third, for a mixed viscosity profile, the IVP analysis reveals that the front initially remains stable, and instability only sets in after a critical time when the reaction has progressed to a sufficient extent. On the contrary, the QSSA predicts the onset of instability right at $t = 0$, which is possibly not accurate.

The diffusivity contrast between the reactants and the product has varied influence on the front's stability, depending on the nature of the viscosity profile. For a monotonically increasing profile, increasing the product's diffusivity has only a small but destabilizing impact on the front. On

the other hand, enhanced diffusivity of the reactant tends to reduce the growth rates because of diminished viscosity gradients assisted by a higher degree of mixing. Conversely, for a mixed viscosity profile, the product's diffusivity has a strong impact on the stability of the front. Indeed, we show that the front can become completely stable when the product diffuses sufficiently fast. An enhanced diffusivity of the reactant in this scenario, however, will lead to increased product formation and hence facilitate the growth of the perturbations, especially at larger times.

One of the main results of this article is how the Péclet number (Pe) impacts the front's stability when hydrodynamic dispersion is accounted for. We show that in the presence of dispersion, the growth rate of the perturbations become largely independent of Pe when it is sufficiently large, regardless of the choice of the viscosity profile. In particular, for a mixed viscosity profile, the onset time of instability as mentioned earlier decreases with Pe in the presence of pure diffusion. However, when hydrodynamic dispersion is active, this onset time eventually becomes independent of Pe for sufficiently large values, in accordance with the conclusion drawn above. This is because for very large values of Pe, mechanical dispersion essentially becomes the only mixing mechanism, while molecular diffusion plays a negligible role. This also explains why the growth rate of the fluctuations continue to depend on Pe when the stability analysis is carried out using pure molecular diffusion.

We hope that the results shown here will provide guiding principles with regard to the spatiotemporal evolution of reactive fronts, relevant to a wide variety of environmental and industrial applications.

ACKNOWLEDGMENTS

G.C. and U.G. gratefully acknowledge the financial support provided for this work by CEFIPRA (IFCPAR), a joint venture by the Government of India and Government of France, through CSRP Project No. 72T09-1. G.C. also acknowledges the director's fellowship provided by IIT Gandhinagar.

DATA AVAILABILITY

The data that support the findings of this article are not publicly available. The data are available from the authors upon reasonable request.

APPENDIX A: DERIVATION OF THE GOVERNING EQUATIONS FOR THE BASE CONCENTRATIONS

For the bimolecular reaction under consideration, the dimensionless transport equations governing the evolution of the reactants and the product are given by Eqs. (7b) and (7c). These equations may be written in the following expanded form:

$$\frac{\partial C_i}{\partial t} + u'\frac{\partial C_i}{\partial x'} + v'\frac{\partial C_i}{\partial y'} = \frac{\partial}{\partial x'}\left(D_{x'x'}\frac{\partial C_i}{\partial x'} + D_{x'y'}\frac{\partial C_i}{\partial y'}\right) + \frac{\partial}{\partial y'}\left(D_{y'x'}\frac{\partial C_i}{\partial x'} + D_{y'y'}\frac{\partial C_i}{\partial y'}\right) - C_A C_B, \quad i \equiv A, B, \tag{A1a}$$

$$\frac{\partial C_C}{\partial t} + u'\frac{\partial C_C}{\partial x'} + v'\frac{\partial C_C}{\partial y'} = \frac{\partial}{\partial x'}\left(D_{x'x'}\frac{\partial C_C}{\partial x'} + D_{x'y'}\frac{\partial C_C}{\partial y'}\right) + \frac{\partial}{\partial y'}\left(D_{y'x'}\frac{\partial C_C}{\partial x'} + D_{y'y'}\frac{\partial C_C}{\partial y'}\right) + C_A C_B. \tag{A1b}$$

In the above, $D_{\alpha\beta}(\alpha,\ \beta \equiv x', y')$ are the components of the nondimensional dispersion tensor given by ($i \equiv A,\ B,\ C$)

$$\mathbf{D}_i = \frac{\Lambda_i}{\mathrm{Pe}}\mathbf{I} + \frac{\eta_L - \eta_T}{((1+u')^2 + v'^2)^{1/2}}\begin{bmatrix} (1+u')^2 & v'(1+u') \\ v'(1+u') & v'^2 \end{bmatrix} + \eta_T((1+u')^2 + v'^2)^{1/2}\mathbf{I}. \tag{A2}$$

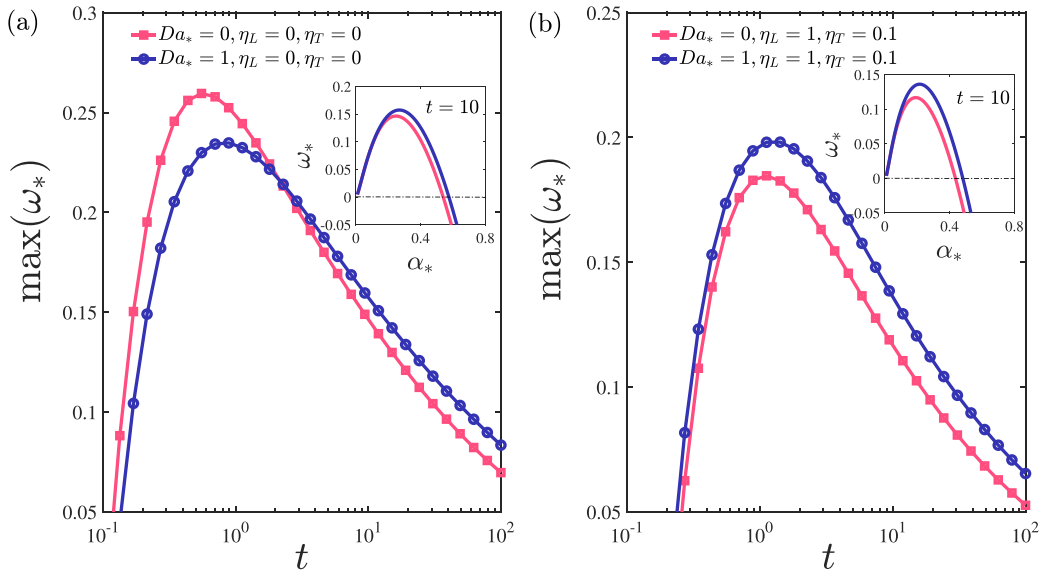

FIG. 14. Variations in the maximum growth rate [max(ω)] vs time (t) (based on the IVP approach) in the case of a monotonically varying viscosity profile with $R_B = 5,\ R_C = 2$ for reactive ($\mathrm{Da}_* = 1$) and nonreactive ($\mathrm{Da}_* = 0$) scenarios under the influence of (a) pure molecular diffusion ($\eta_L = \eta_T = 0$) and (b) anisotropic dispersion with $\eta_L = 1,\ \eta_T = 0.1$. The respective insets show the dispersion curves at $t = 10$. Values of other parameters are $\mathrm{Pe} = 1,\ \Lambda_B = \Lambda_C = 1$. In all cases, Eqs. (22) have been solved, and reference scales as described in Sec. III F have been adopted.

Now, in the absence of any disturbances, the flow field remains spatially uniform, and its magnitude is equal to the injection velocity of reactant A (which is unity in the present dimensionless formulation). Consequently, the dispersion tensor in Eq. (A2) simplifies to the following form:

$$\mathbf{D}_i = \begin{bmatrix} \frac{\Lambda_i}{\mathrm{Pe}} + \eta_L & 0 \\ 0 & \frac{\Lambda_i}{\mathrm{Pe}} + n_T \end{bmatrix}. \tag{A3}$$

Substituting the above expression for the dispersion tensor into Eqs. (A1a) and (A1b), and noting that the species concentrations in the base-state depend only on (x') and (t) for a spatially uniform velocity field (i.e., $\partial C_i/\partial y' = 0$), the governing equations for the base-state concentrations reduce to Eqs. (11a)–(11c).

APPENDIX B: COMPARISON OF THE REACTIVE AND NONREACTIVE SCENARIOS FOR A MONOTONICALLY INCREASING VISCOSITY PROFILE ($R_B > R_C > 0$)

It is obvious that the monotonically increasing viscosity profile ($\mu_A < \mu_C < \mu_B$) is inherently unstable, i.e., even a nonreactive mixing front between species A and B will be prone to viscous fingering instabilities. Formation of the product also maintains conditions favorable to viscous fingering, although it reduces the viscosity gradient across the front simply because $\mu_C < \mu_B$. Therefore, one question that naturally arises here is does the reaction actually facilitate instability or reduce its intensity? We answer this question in Fig. 14, where the maximum growth rates (max(ω), computed using the IVP approach) for the reactive ($\mathrm{Da}_* = 1$) and nonreactive scenarios ($\mathrm{Da}_* = 0$), are compared when the viscosity profile varies monotonically ($R_B = 5,$ and $R_C = 2$) with $\mathrm{Pe} = 1$. Panel (a) shows this comparison in the absence of dispersion ($\eta_L = \eta_T = 0$), and panel (b) shows the same comparison for anisotropic dispersion ($\eta_L = 1$, and $\eta_T = 0.1$). The corresponding insets

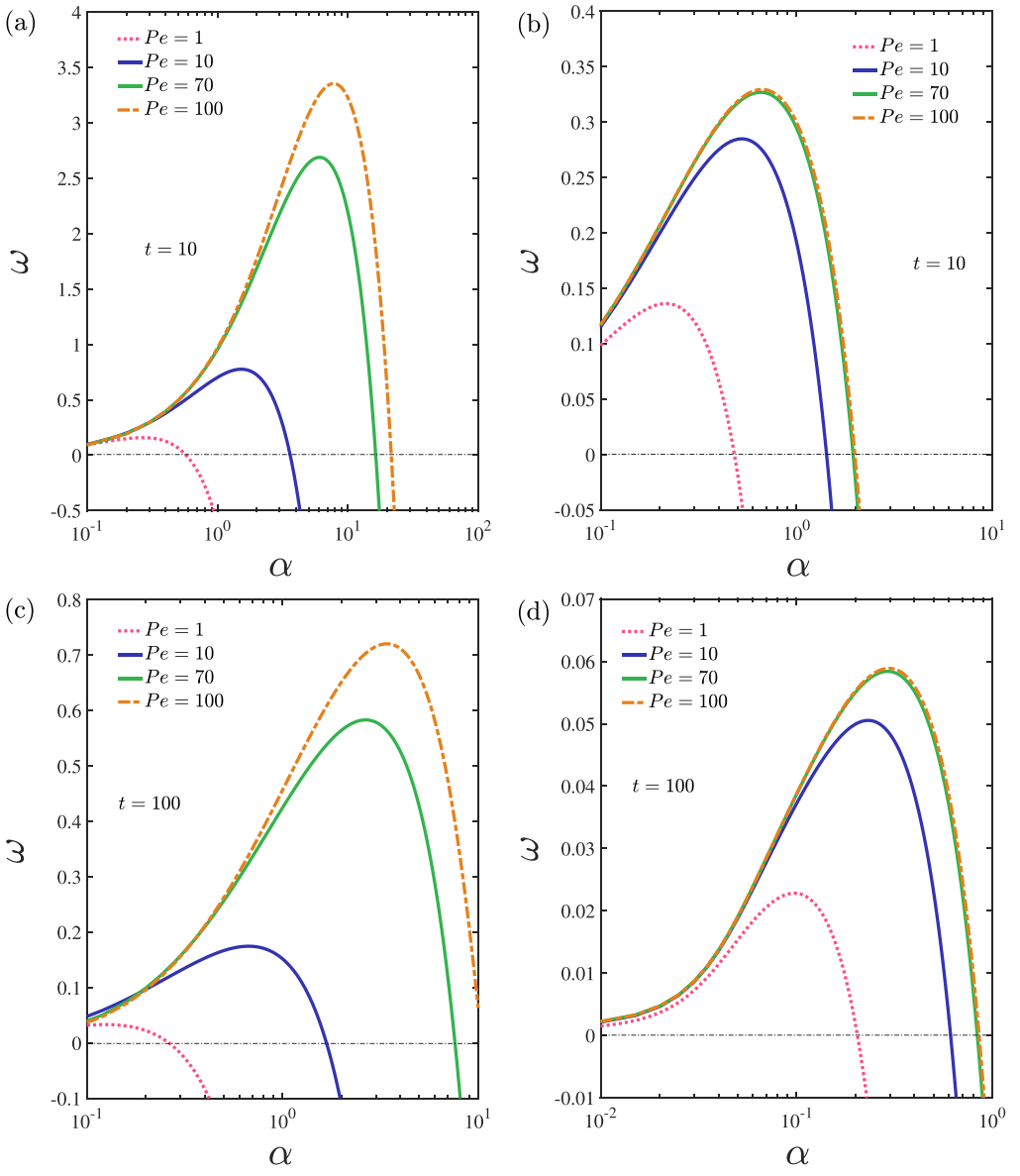

FIG. 15. Dispersion curves (ω vs α) based on the IVP approach for (a), (c) pure diffusion and (b), (d) anisotropic dispersion ($\eta_L = 1$, and $\eta_T = 0.1$) with varying Pe $= 1,\ 10,\ 70,\ 100$. (a), (b) For the monotonic viscosity profile ($R_B = 5$ and $R_C = 2$) at time $t = 10$; (c), (d) corresponding results for a mixed viscosity profile ($R_B = -2$ and $R_C = 5$) at time $t = 100$. Other parameters are $\Lambda_B = \Lambda_C = 1$.

display the dispersion curves at $t = 10$. The values of all other relevant parameters are provided in the figure caption.

It is important to mention that, because we compare reactive and nonreactive scenarios in the same figure, the timescales outlined in Table I will not work here, simply because the reaction time does not exist in the nonreactive scenario. Therefore, for the purposes of Fig. 14, we have chosen the reference scales identical to those of Hejazi *et al.* [26], also mentioned in Sec. III F. Thus, the

linearized equations now take the form given in Eqs. (22), which were solved numerically using the same method as outlined in Sec. III E. It is evident from Fig. 14(a) that under pure diffusion, the reaction tends to suppress the growth of the perturbations at early times, although later it enhances the growth rate. On the other hand, in the presence of dispersion [Fig. 14(b)], the reaction always tends to enhance the growth rate of the perturbations. The reason for the above observation possibly stems from the fact that in a nonreactive front, there will only be a single mixing front which will be the sole driver of instability. On the other hand, in the presence of reaction, the front has two faces [also see Fig. 3(a)], both of which are unstable and hence may promote the growth of the disturbances to a greater extent, especially after the reaction has progressed to a significant extent. Since dispersion enhances mixing and hence facilitates product formation, this explains why, in the presence of dispersion, the growth rates are always enhanced by the chemical reaction. For the purely diffusive case, such amplification becomes appreciable only at relatively later times. It is also observed that the presence of hydrodynamic dispersion [compare Figs. 14(a) and 14(b)] has a stabilizing influence with respect to pure diffusion. This is in full agreement with what was observed for a reactive front in Figs. 6(a) and 6(c).

APPENDIX C: IMPACT OF *Pe* UNDER PURE DIFFUSION AND HYDRODYNAMIC DISPERSION

Under identical diffusivity ratios, the mixing of species at the interfaces is governed by both the Péclet number and the dispersion length (η_L and η_T). Figure 15 compares the impact of Pe on the dispersion curves obtained using the IVP analysis, for the case of pure diffusion [Figs. 15(a) and 15(c)] and for anisotropic dispersion with $\eta_L = 1$ and $\eta_T = 0.1$ [Figs. 15(b) and 15(d)]. Figures 15(a) and 5(b) depict the results for a monotonic viscosity profile ($R_B = 5$ and $R_C = 2$), and those in Figs. 15(c) and 15(d) are for the mixed viscosity profile ($R_B = -2$ and $R_C = 5$). The values of other relevant parameters have been mentioned in the figure caption. In the absence of dispersion ($\eta_L = \eta_T = 0$), mixing is solely governed by Pe (i.e., diffusion). A relatively larger Pe implies reduced mixing (and hence a more prominent viscosity contrast in an already unstable scenario) and is therefore expected to promote the growth of perturbations. This is exactly what is observed in Figs. 15(a) and 15(c), where increasing Pe leads to a monotonic increase in the peak growth rates as well as the range of unstable wave numbers. On the contrary, in the presence of dispersion, beyond a sufficiently large Pe, diffusion has negligible impact on the proceedings and hence the perturbations become independent of Pe—also see the discussion related to Fig. 13. This is also reflected in the dispersion curves shown in Figs. 15(c) and 15(d), where ω as well as the range of unstable wave numbers become Pe independent when Pe $\geqslant 70$. Finally, it is also worth noting that the growth rates of the perturbations seem to be more sensitive to Pe in the case of a monotonic viscosity profile, simply because this configuration is inherently unstable.

[1] P. K. Kitanidis and P. L. McCarty, *Delivery and Mixing in the Subsurface: Processes and Design Principles for In Situ Remediation* (Springer Science & Business Media, New York, 2012), Vol. 4.

[2] A. Faisal, A. Sulaymon, and Q. Khaliefa, A review of permeable reactive barrier as passive sustainable technology for groundwater remediation, Int. J. Environ. Sci. Technol. **15**, 1123 (2018).

[3] S. Mohammadian, B. Krok, A. Fritzsche, C. Bianco, T. Tosco, E. Cagigal, B. Mata, V. Gonzalez, M. Diez-Ortiz, V. Ramos, *et al.*, Field-scale demonstration of in situ immobilization of heavy metals by injecting iron oxide nanoparticle adsorption barriers in groundwater, J. Contam. Hydrol. **237**, 103741 (2021).

[4] M. A. Mahardika, Y. She, F. Shori, A. Patmonoaji, S. Matsushita, T. Suekane, and Y. Nagatsu, Enhanced heavy oil recovery by calcium hydroxide flooding with the production of viscoelastic materials: Study with 3-D x-ray tomography and 2-D glass micromodels, Energy Fuels **35**, 11210 (2021).

[5] A. Muggeridge, A. Cockin, K. Webb, H. Frampton, I. Collins, T. Moulds, and P. Salino, Recovery rates, enhanced oil recovery and technological limits, Philos. Trans. R. Soc. A **372**, 20120320 (2014).
[6] J. Jiménez-Martínez, M. L. Porter, J. D. Hyman, J. W. Carey, and H. S. Viswanathan, Mixing in a three-phase system: Enhanced production of oil-wet reservoirs by CO_2 injection, Geophys. Res. Lett. **43**, 196 (2016).
[7] F. Liu, P. Lu, C. Zhu, and Y. Xiao, Coupled reactive flow and transport modeling of CO_2 sequestration in the Mt. Simon sandstone formation, Midwest USA, Int. J. Greenhouse Gas Control **5**, 294 (2011).
[8] M. L. Szulczewski, C. W. MacMinn, H. J. Herzog, and R. Juanes, Lifetime of carbon capture and storage as a climate-change mitigation technology, Proc. Natl. Acad. Sci. **109**, 5185 (2012).
[9] K. Gautam and P. Narayana, On the stability of carbon sequestration in an anisotropic horizontal porous layer with a first-order chemical reaction, Proc. R. Soc. A **475**, 20180365 (2019).
[10] M. Addassi, A. Omar, H. Hoteit, A. M. Afifi, S. Arkadakskiy, Z. T. Ahmed, N. Kunnummal, S. R. Gislason, and E. H. Oelkers, Assessing the potential of solubility trapping in unconfined aquifers for subsurface carbon storage, Sci. Rep. **12**, 20452 (2022).
[11] A. M. Tartakovsky, G. D. Tartakovsky, and T. D. Scheibe, Effects of incomplete mixing on multicomponent reactive transport, Adv. Water Resour. **32**, 1674 (2009).
[12] M. Dentz, T. Le Borgne, A. Englert, and B. Bijeljic, Mixing, spreading and reaction in heterogeneous media: A brief review, J. Contam. Hydrol. **120-121**, 1 (2011).
[13] M. Rolle and T. Le Borgne, Mixing and reactive fronts in the subsurface, Rev. Mineral. Geochem. **85**, 111 (2019).
[14] R. Tarkowski, Underground hydrogen storage: Characteristics and prospects, Renewable Sustainable Energy Rev. **105**, 86 (2019).
[15] L. Stolze and M. Rolle, Surface complexation reactions in sandy porous media: Effects of incomplete mixing and mass-transfer limitations in flow-through systems, J. Contam. Hydrol. **246**, 103965 (2022).
[16] X. Zhang, Z. Dou, M. Hamada, P. de Anna, and J. Jimenez-Martinez, Enhanced reaction kinetics in stationary two-phase flow through porous media, Environ. Sci. Technol. **59**, 1334 (2025).
[17] J. Fernandez and G. Homsy, Viscous fingering with chemical reaction: Effect of *in-situ* production of surfactants, J. Fluid Mech. **480**, 267 (2003).
[18] Y. Nagatsu, K. Matsuda, Y. Kato, and Y. Tada, Experimental study on miscible viscous fingering involving viscosity changes induced by variations in chemical species concentrations due to chemical reactions, J. Fluid Mech. **571**, 475 (2007).
[19] Y. Nagatsu, Y. Kondo, Y. Kato, and Y. Tada, Effects of moderate Damköhler number on miscible viscous fingering involving viscosity decrease due to a chemical reaction, J. Fluid Mech. **625**, 97 (2009).
[20] C. Almarcha, P. Trevelyan, L. A. Riolfo, A. Zalts, C. El Hasi, A. D'Onofrio, and A. De Wit, Active role of a color indicator in buoyancy-driven instabilities of chemical fronts, J. Phys. Chem. Lett. **1**, 752 (2010).
[21] S. Kuster, L. A. Riolfo, A. Zalts, C. El Hasi, C. Almarcha, P. Trevelyan, A. De Wit, and A. D'Onofrio, Differential diffusion effects on buoyancy-driven instabilities of acid–base fronts: The case of a color indicator, Phys. Chem. Chem. Phys. **13**, 17295 (2011).
[22] A. De Wit, Chemo-hydrodynamic patterns and instabilities, Annu. Rev. Fluid Mech. **52**, 531 (2020).
[23] T. Podgorski, M. C. Sostarecz, S. Zorman, and A. Belmonte, Fingering instabilities of a reactive micellar interface, Phys. Rev. E **76**, 016202 (2007).
[24] S. Sin, T. Suekane, Y. Nagatsu, and A. Patmonoaji, Three-dimensional visualization of viscous fingering for non-Newtonian fluids with chemical reactions that change viscosity, Phys. Rev. Fluids **4**, 054502 (2019).
[25] S. Hirano, Y. Nagatsu, and R. X. Suzuki, Reversal of effects from gel production in a reacting flow dependent on gel strength, Phys. Rev. Fluids **7**, 023201 (2022).
[26] S. Hejazi, P. Trevelyan, J. Azaiez, and A. De Wit, Viscous fingering of a miscible reactive $A + B \rightarrow C$ interface: A linear stability analysis, J. Fluid Mech. **652**, 501 (2010).
[27] F. Brau, G. Schuszter, and A. De Wit, Flow control of $A+ B\rightarrow C$ fronts by radial injection, Phys. Rev. Lett. **118**, 134101 (2017).
[28] B. Dastvareh and J. Azaiez, Instabilities of nonisothermal nanocatalytic reactive flows in porous media, Phys. Rev. Fluids **4**, 034003 (2019).

[29] A. Kumar and M. Mishra, Nanoparticles impact on miscible viscous fingering with absorbing boundary condition at inlet, Phys. Rev. Fluids **7**, 044001 (2022).
[30] V. Sharma, C.-Y. Chen, and M. Mishra, A linear stability analysis of instabilities with reactive flows in porous medium, Phys. Fluids **35**, 064105 (2023).
[31] A. De Wit and G. Homsy, Nonlinear interactions of chemical reactions and viscous fingering in porous media, Phys. Fluids **11**, 949 (1999).
[32] A. De Wit and G. Homsy, Viscous fingering in reaction-diffusion systems, J. Chem. Phys. **110**, 8663 (1999).
[33] T. Gérard and A. De Wit, Miscible viscous fingering induced by a simple $A + B \rightarrow C$ chemical reaction, Phys. Rev. E **79**, 016308 (2009).
[34] Y. Nagatsu and A. De Wit, Viscous fingering of a miscible reactive $A + B \rightarrow C$ interface for an infinitely fast chemical reaction: Nonlinear simulations, Phys. Fluids **23**, 043103 (2011).
[35] V. Sharma, S. Pramanik, C.-Y. Chen, and M. Mishra, A numerical study on reaction-induced radial fingering instability, J. Fluid Mech. **862**, 624 (2019).
[36] R. Tsuzuki, Q. Li, Y. Nagatsu, and C.-Y. Chen, Numerical study of immiscible viscous fingering in chemically reactive Hele-Shaw flows: Production of surfactants, Phys. Rev. Fluids **4**, 104003 (2019).
[37] P. Shukla and A. De Wit, Influence of the Péclet number on reactive viscous fingering, Phys. Rev. Fluids **5**, 014004 (2020).
[38] P. Verma, V. Sharma, C.-Y. Chen, and M. Mishra, Damköhler number independent stable regime in reactive radial viscous fingering, J. Fluid Mech. **1000**, A72 (2024).
[39] K. Ghesmat and J. Azaiez, Miscible displacements of reactive and anisotropic dispersive flows in porous media, Transp. Porous Media **77**, 489 (2009).
[40] P. Jangir, R. Mohan, and P. Chokshi, Numerical study on nonisothermal reactive viscous fingering, Chem. Eng. Sci. **285**, 119533 (2024).
[41] J. Bear and A. H.-D. Cheng, *Modeling Groundwater Flow and Contaminant Transport* (Springer, Dordrecht, 2010), Vol. 23.
[42] P. Saffman, A theory of dispersion in a porous medium, J. Fluid Mech. **6**, 321 (1959).
[43] S. Whitaker, *The Method of Volume Averaging*, Theory and Applications of Transport in Porous Media (Springer Science & Business Media, Dordrecht, 2013), Vol. 13.
[44] L. de Arcangelis, J. Koplik, S. Redner, and D. Wilkinson, Hydrodynamic dispersion in network models of porous media, Phys. Rev. Lett. **57**, 996 (1986).
[45] B. Bijeljic, P. Mostaghimi, and M. J. Blunt, Signature of non-Fickian solute transport in complex heterogeneous porous media, Phys. Rev. Lett. **107**, 204502 (2011).
[46] R. M. Neupauer, L. J. Sather, D. C. Mays, J. P. Crimaldi, and E. J. Roth, Contributions of pore-scale mixing and mechanical dispersion to reaction during active spreading by radial groundwater flow, Water Resour. Res. **56**, e2019WR026276 (2020).
[47] P. Karan, U. Ghosh, F. Brau, Y. Méheust, and T. Le Borgne, Effect of hydrodynamic dispersion on spherical reaction front dynamics in porous media, Phys. Rev. Fluids **8**, 084502 (2023).
[48] P. Karan, U. Ghosh, Y. Méheust, and T. Le Borgne, Impact of hydrodynamic dispersion on mixing-induced reactions under radial flows, Adv. Water Resour. **179**, 104521 (2023).
[49] G. Rousseau, S. Izumoto, T. Le Borgne, and J. Heyman, Dispersion versus diffusion in mixing fronts, Water Resour. Res. **59**, e2023WR035848 (2023).
[50] S. Izumoto, G. Rousseau, T. Le Borgne, and J. Heyman, Effective reaction kinetics of steady mixing fronts in porous media, J. Fluid Mech. **1013**, A4 (2025).
[51] R. Benhammadi, P. Meunier, and J. J. Hidalgo, Experimental and numerical study of CO_2 dissolution in a heterogeneous Hele-Shaw cell, Phys. Rev. Fluids **10**, 043501 (2025).
[52] G. Chakraborty, P. Karan, Y. Méheust, T. Le Borgne, and U. Ghosh, Reactive fronts dynamics under joint shear deformation and hydrodynamic dispersion, Adv. Water Resour. **211**, 105269 (2026).
[53] B. Wen, K. W. Chang, and M. A. Hesse, Rayleigh-Darcy convection with hydrodynamic dispersion, Phys. Rev. Fluids **3**, 123801 (2018).
[54] Y. C. Yortsos and M. Zeybek, Dispersion driven instability in miscible displacement in porous media, Phys. Fluids **31**, 3511 (1988).

[55] K. Ghesmat and J. Azaiez, Viscous fingering instability in porous media: Effect of anisotropic velocity-dependent dispersion tensor, Transp. Porous Media **73**, 297 (2008).
[56] M. Mishra, P. M. J. Trevelyan, C. Almarcha, and A. De Wit, Influence of double diffusive effects on miscible viscous fingering, Phys. Rev. Lett. **105**, 204501 (2010).
[57] M. B. Cil, M. Xie, A. I. Packman, and G. Buscarnera, Solute mixing regulates heterogeneity of mineral precipitation in porous media, Geophys. Res. Lett. **44**, 6658 (2017).
[58] F. Brau and A. De Wit, Influence of rectilinear vs radial advection on the yield of A+ B→ C reaction fronts: A comparison, J. Chem. Phys. **152**, 054716 (2020).
[59] M. Arshadi and H. Rajaram, Transport with bimolecular reactions in a fracture-matrix system: Analytical solutions with applications to in situ chemical oxidation, Water Resour. Res. **55**, 3904 (2019).
[60] U. Ghosh, T. Borgne, D. Jougnot, N. Linde, and Y. Méheust, Geoelectrical signatures of reactive mixing: A theoretical assessment, Geophys. Res. Lett. **45**, 3489 (2018).
[61] J. Bear, *Dynamics of Fluidsl in Porous Media* (Courier Corporation, Mineola, NY, 2013).
[62] G. I. Taylor, Dispersion of soluble matter in solvent flowing slowly through a tube, Proc. R. Soc. London A **219**, 186 (1953).
[63] C. T. Tan and G. M. Homsy, Stability of miscible displacements in porous media: Rectilinear flow, Phys. Fluids **29**, 3549 (1986).
[64] Y. Ben, E. A. Demekhin, and H.-C. Chang, A spectral theory for small-amplitude miscible fingering, Phys. Fluids **14**, 999 (2002).
[65] M. C. Kim and C. K. Choi, The stability of miscible displacement in porous media: Nonmonotonic viscosity profiles, Phys. Fluids **23**, 084105 (2011).
[66] S. Pramanik, T. K. Hota, and M. Mishra, Influence of viscosity contrast on buoyantly unstable miscible fluids in porous media, J. Fluid Mech. **780**, 388 (2015).
[67] T. K. Hota, S. Pramanik, and M. Mishra, Onset of fingering instability in a finite slice of adsorbed solute, Phys. Rev. E **92**, 023013 (2015).
[68] T. K. Hota and M. Mishra, Non-modal stability analysis of miscible viscous fingering with non-monotonic viscosity profiles, J. Fluid Mech. **856**, 552 (2018).
[69] P. J. Schmid, D. S. Henningson, and D. Jankowski, *Stability and Transition in Shear Flows*, Applied Mathematical Sciences Vol. 142 (Springer, New York, 2002).
[70] C. Pozrikidis, *Introduction to Theoretical and Computational Fluid Dynamics* (Oxford University Press, 2011).
[71] J. P. Boyd, *Chebyshev and Fourier Spectral Methods* (Courier Corporation, Mineola, NY, 2001).
[72] L. N. Trefethen, *Spectral Methods in MATLAB, Software, Environments, and Tools* (Society for Industrial and Applied Mathematics, Philadelphia, PA, 2000), Vol. 10.
[73] B. Bijeljic and M. J. Blunt, Pore-scale modeling of transverse dispersion in porous media, Water Resour. Res. **43**, 2006WR005700 (2007).
[74] J. Azaiez and M. Sajjadi, Stability of double-diffusive double-convective miscible displacements in porous media, Phys. Rev. E **85**, 026306 (2012).
[75] M. C. Kim, Double diffusive effects on radial fingering in a porous medium or a Hele-Shaw cell, Korean J. Chem. Eng. **35**, 364 (2018).